

Distributed control of motor circuits for backward walking in *Drosophila*

Kai Feng ^{1✉}, Rajyashree Sen ^{2,4}, Ryo Minegishi ², Michael Dübbert ³, Till Bockemühl ³, Ansgar Büschges ³ & Barry J. Dickson ^{1,2✉}

How do descending inputs from the brain control leg motor circuits to change how an animal walks? Conceptually, descending neurons are thought to function either as command-type neurons, in which a single type of descending neuron exerts a high-level control to elicit a coordinated change in motor output, or through a population coding mechanism, whereby a group of neurons, each with local effects, act in combination to elicit a global motor response. The *Drosophila* Moonwalker Descending Neurons (MDNs), which alter leg motor circuit dynamics so that the fly walks backwards, exemplify the command-type mechanism. Here, we identify several dozen MDN target neurons within the leg motor circuits, and show that two of them mediate distinct and highly-specific changes in leg muscle activity during backward walking: LBL40 neurons provide the hindleg power stroke during stance phase; LUL130 neurons lift the legs at the end of stance to initiate swing. Through these two effector neurons, MDN directly controls both the stance and swing phases of the backward stepping cycle. These findings suggest that command-type descending neurons can also operate through the distributed control of local motor circuits.

¹Queensland Brain Institute, University of Queensland, St Lucia, QLD 4072, Australia. ²Janelia Research Campus, Howard Hughes Medical Institute, 19700 Helix Drive, Ashburn, VA 20147, USA. ³Institute for Zoology, Biocenter Cologne, University of Cologne, D-50674 Cologne, Germany. ⁴Present address: The Mortimer B. Zuckerman Mind Brain Behavior Institute, Department of Neuroscience, Columbia University, New York, NY 10027, USA. ✉email: k.feng@uq.edu.au; b.dickson@uq.edu.au

The simple act of walking appears effortless, yet involves the exquisitely timed and scaled activation of multiple muscles in each leg. The motor circuits that produce these muscle movements are controlled by descending inputs from the brain and sensory feedback from the legs^{1,2}. The descending inputs modulate the overall locomotor pattern, effecting changes in direction or pace in accordance with the animal's behavioral goals^{3,4}. Sensory feedback, including both external and proprioceptive signals, coordinate progression through the stepping cycle and make the fine adjustments needed to adapt to a varying terrain⁵. While this overall organization is now well established, we still have only very limited understanding of how such descending and peripheral inputs control locomotor circuits⁶. Determining how descending and peripheral inputs control motor circuits for walking thus remains an important open question in basic neuroscience, with the potential to inform approaches in human therapy⁷ and robotics⁸.

One of the most striking descending controls of leg motor circuits effects a transition from forward to backward walking. Virtually all animals are capable of walking backwards, albeit with varying degrees of elegance. The most obvious change in leg kinematics in backward walking is the phase switch in leg movements—from the leg moving forward in swing phase and backward in stance phase, to forward in stance phase and backward in swing phase. Yet backward walking involves much more than just a simple phase switch, as the amplitude and speed of movement at each joint must also be altered for smooth backward propulsion^{9,10}. Additionally, for animals with multiple pairs of legs, the hindlegs rather than the forelegs are now the first to encounter the oncoming terrain. The transition to backward walking thus provides an excellent paradigm to explore the more general question of how descending inputs from the brain make the myriad adjustments in motor circuits necessary to effect a smooth and coordinated change in walking direction.

Here we begin to investigate the descending control of locomotor circuits for backward walking in *Drosophila*. Flies, like many other animals, retreat if they perceive a threat or obstacle in the path ahead. These sensory cues are believed to act primarily through a single class of descending neurons, called the Moon-walker Descending Neurons (MDNs), which act as command-type neurons for backward walking¹¹. Flies with genetically silenced MDNs are unable to walk backwards when they encounter a physical obstacle. Conversely, freely roaming flies walk backwards if the MDNs are artificially activated¹¹. MDNs receive input from neurons conveying mechanosensory cues¹² (representing a possible obstacle) and from visual neurons that detect a looming stimulus¹³ (a potential threat). The MDNs are also present in larvae, where they mediate backward crawling¹⁴. Presumably, MDNs control very different motor circuits in the larvae and adult, as the former produce peristaltic waves of the body wall musculature whereas the latter generate the stepping action of legs. While some progress has been made in identifying the larval motor circuits that the MDNs engage for backward crawling¹⁴, the motor circuits they activate in the adult for backward walking remain unknown.

By studying leg joint kinematics, we found that the adult MDNs drive coordinated changes in stepping patterns across all three pairs of legs, with the strongest impact on the hindlegs. By combining anatomical and functional approaches, we identify several dozen morphologically distinct candidate MDN target cell types in the ventral nerve cord (VNC). Using cell-type specific genetic drivers, we confirmed that many of these cell types are indeed required for backward walking, and analyzed two of them in detail. The LBL40 neurons—specific to the T3 segment—mediate tibia flexion during the power stroke of backward walking. The LUL130 neurons—present in all segments but

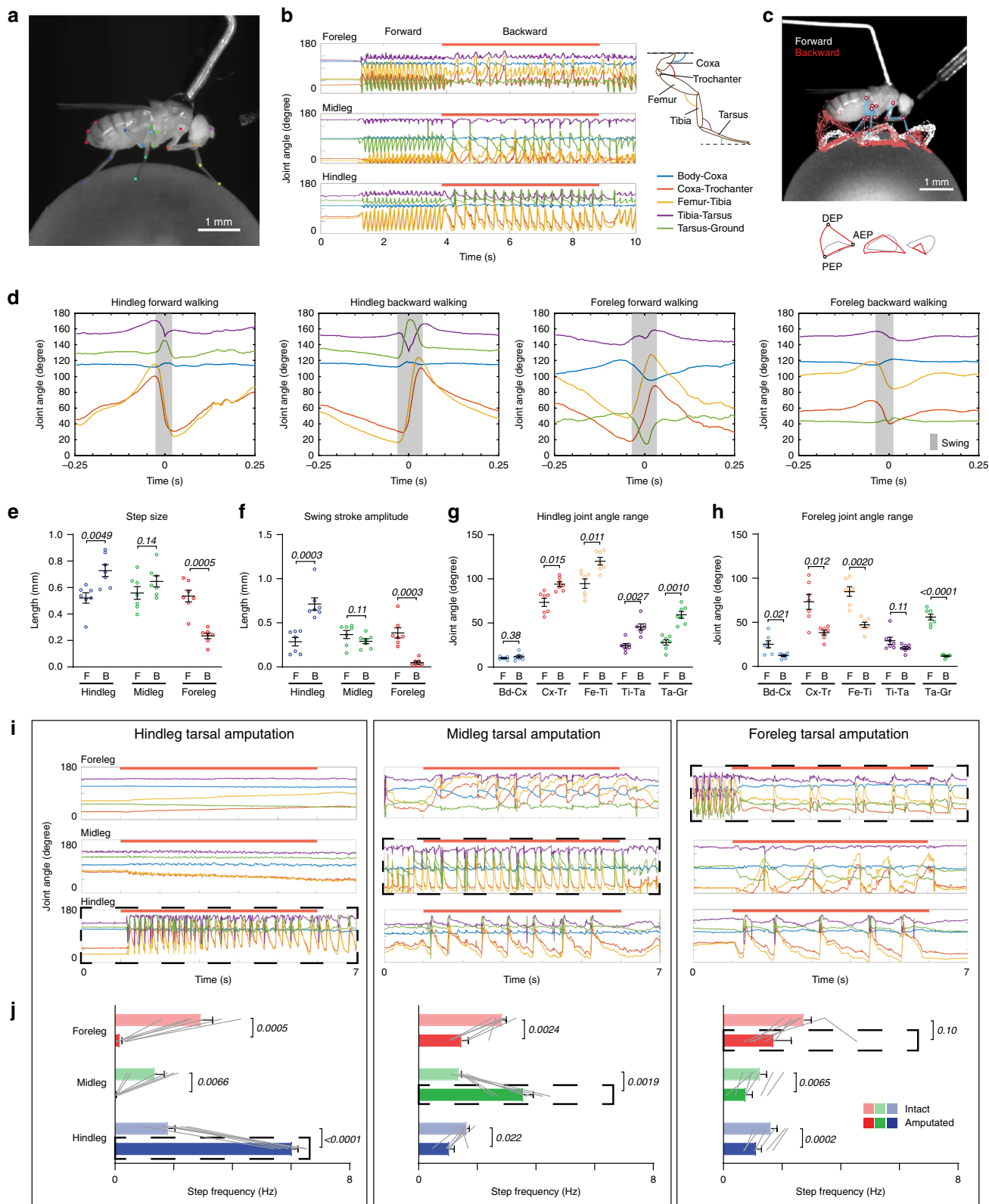
activated by MDN most strongly in T3—lift the hindlegs to initiate swing phase. These two MDN-effector neurons thus mediate two critical hindleg movements in backward walking: the power stroke during stance phase (LBL40) and elevation at the start of swing phase (LUL130).

Models for the descending control of motor circuits have generally emphasized either of two extreme scenarios: a command-type of control, in which a single type of descending neuron, like MDN, effects a coordinated set of changes of many muscle movements, versus a more distributed, population-type of control, in which a single type of descending neuron modulates a limited set of motor outputs, with many such descending inputs working in combination to produce a coordinated pattern of muscle movements. Intuitively, command-type descending neurons might be expected to exert a relatively high-level, centralized control on motor circuits, whereas population-type descending neurons might impinge at a lower level, close to the specific motor outputs they control. Our analysis of MDN outputs suggests, however, that command-type neurons can also act in a highly distributed and localized manner: We propose that MDN acts as a command-type neuron because its distributed outputs collectively effect a state switch in motor circuit network dynamics—from a resting or forward walking state to a backward walking state.

Results

Joint kinematics suggest that hindlegs dominate MDN-triggered backward walking. Before embarking on a detailed investigation of how MDN couples to leg motor circuits, we first sought to better understand how MDN activation impacts leg movements. Previous studies of MDN-triggered backward walking have examined only the translocation of the body^{11–13} or the pattern of footfalls¹¹. To determine how MDN alters leg joint kinematics, we acquired high-speed (200 fps) videos of tethered flies walking on a suspended ball¹⁵, and used the DeepLabCut software¹⁶ to train a neural network to automatically detect the positions of each leg joint (Fig. 1a and Supplementary Movie 1). Each of the 6 legs has 4 highly articulated joints. From proximal to distal, these are the body-coxa, coxa-trochanter, femur-tibia, and tibia-tarsus joints (Fig. 1b). In *Drosophila*, as in many other insects¹⁷, the trochanter-femur joint has limited mobility). These joints, as well as the tarsal tips, were located for all three legs on one side of the body in each video frame (Fig. 1a, b). We analyzed videos of both spontaneous forward walking and MDN-triggered backward walking (Fig. 1b–h).

The trajectories of the tarsal tips differed considerably during bouts of forward and backward walking by the same fly (Fig. 1c and Supplementary Movie 1). The forelegs stepped further and higher when walking forwards than when walking backwards; the hindlegs took longer and higher strides when walking backwards (Fig. 1c–f). The fore- and hindlegs are generally oriented parallel to the fly's body axis, and so the lateral placement of our video camera provides the best perspective for tracking joint angles in these legs. We found that the two joints with the greatest range of motion in both forward and backward walking were the coxa-trochanter and femur-tibia joints (Fig. 1b, d, g, h). The flexion and extension of these two joints occurred synchronously for each leg, but in opposite stepping phases for forelegs versus hindlegs (Fig. 1d). During forward walking, the foreleg coxa-trochanter and femur-tibia joints were flexed in stance phase and extended in swing phase; the hindleg joints were flexed in swing and extended in stance. The phase coupling of flexion and extension was reversed during MDN-triggered backward walking. Thus, the forelegs appear to pull the body forward during forward walking, with the hindlegs either pushing or passively extending.



For backward walking, the hindlegs pull, while the forelegs either push or passively extend. Regardless of which direction the fly walks, the leading legs take the higher steps, which may facilitate walking on uneven terrain or over obstacles.

To assess whether the hindlegs indeed provide the greatest propulsive force during backward walking, we next performed a series of amputation experiments. In these experiments, we first

monitored leg joint kinematics in an intact fly upon MDN activation, then bilaterally amputated the tarsal tips from one pair of legs before again activating MDN and videotaping leg movements. Tarsal amputation prevents the leg from gaining any traction on the ground but preserves all the leg joints. We found that the fore- and midleg amputees were still able to walk backwards, whereas the hindleg amputees could not (Fig. 1i, j and

Fig. 1 Joint kinematics during forward and backward walking. **a** An example frame from high-speed videos of fly walking on a 6-mm diameter ball. Colored dots indicate anatomical landmarks annotated by an artificial neural network trained on DeepLabCut. **b** Right, schematic of a *Drosophila* leg showing each leg segment and joint, and color codes used for each joint in all Figures. Left, joint angle tracking from an episode of an MDN > CsChrimson fly walking on ball. Red bars indicate the red-light stimulus. **c** Top, a frame from the Supplementary Movie 1 tracked in **b**, overlaid with the trajectory of tarsal tips of all three legs during forward walking (white) and backward walking (red). Bottom, average trajectories of tarsal tips during forward walking (gray) and backward walking (red). Anterior (AEP), posterior (PEP), and dorsal (DEP) extreme positions for the hindleg are indicated. See also Supplementary Movie 1. **d** Joint angles from averaged steps of hindleg and foreleg during forward walking and backward walking. Grey shading represents swing phase, as inferred from the averaged tarsal tip trajectories. $N = 7$ flies; $n = 156, 75, 156, \text{ or } 142$ steps (from left to right). **e** Average step size for each fly during forward and backward walking, defined as the distance between AEP and PEP. F forward walking, B backward walking. Bars indicate mean \pm s.e.m. of per fly averages for **e-h**. **f** Average swing stroke amplitude, defined as the distance between DEP and the line segment connecting AEP and PEP. **g** Average foreleg joint angle range (maximum–minimum angle). **h** Average hindleg joint angle range. **i** Representative joint angle tracking of flies with fore-, mid-, or hindlegs bilaterally amputated at the tarsus. Dashed boxes indicate the amputated leg. See also Supplementary Movie 2. **j** Stepping frequency for each leg, before and after amputation, shown as mean \pm s.e.m. $n = 6$ flies for each group. Grey lines indicate paired trial averages for the same fly, before and after amputation. *P* values are shown in italics; two-tailed paired *t*-tests. Source data are provided as a Source Data file.

Supplementary Movie 2). Thus, it is primarily the stance phase power stroke of the hindleg that drives the body backwards when MDN is activated. Interestingly, in all cases, the amputated legs continued to oscillate, suggesting that their stepping motion is actively driven by central motor circuits and not merely a passive consequence of their surface traction (Fig. 1i, j and Supplementary Movie 2). We also noticed that, particularly for the hindlegs, but to a lesser extent also the midlegs, the stepping frequency even increased upon amputation, as if they were continually seeking surface contact (Fig. 1j).

We conclude from this series of experiments that MDN induces backward walking predominantly by engaging the muscles that control the hindleg coxa-trochanter and femur-tibia joints. MDN switches the phases of flexion and extension for these joints during the stepping cycle, and enhances their movement in the hindleg so as to mirror those of the corresponding foreleg joints during forward walking. As a result of these adjustments to hindleg stepping, it is the hindlegs that provide the main propulsive force during backward walking. MDN likely also provides neural input to the midleg and foreleg motor circuits. However, MDN's impact in these segments is considerably weaker and, in the absence of any drive from the hindlegs, insufficient to propel the animal backwards.

Trans-Tango reveals cells postsynaptic to MDNs. Having determined how MDN activation changes leg kinematics, we next sought to trace the neural circuits through which MDN effects these changes. In a first approach, we used the trans-Tango method¹⁸ to identify cells in the VNC likely to be postsynaptic to MDNs. Trans-Tango employs a heterologous ligand to activate its cognate receptor in postsynaptic cells, which then become labeled by expression of a QF-dependent reporter. We targeted the trans-Tango ligand to MDNs and the trans-Tango receptor to all neurons, and acquired confocal images of the VNC to visualize postsynaptic cells labeled by an mtdTomato-3HA reporter (Fig. 2a). A large number of cells in the VNC were MDN trans-Tango-positive, and, as expected, their neurites overlap extensively with the axonal arborizations of the MDNs in all three leg neuropils (Fig. 2a). This high density of trans-Tango labeling precluded the identification of individual cell types. In order to visualize single trans-Tango-positive cells, we therefore used a stochastic variant of trans-Tango¹⁸ in which only a small subset of the postsynaptic cells were labeled in any one sample (Fig. 2b). A total of 541 samples were imaged by confocal microscopy and registered onto a common reference template (ref. ¹⁹; Fig. 2b).

The cell types labeled by trans-Tango were highly diverse in their morphology. We identified 65 morphologically distinct cell types amongst the 541 samples, and segmented a representative cell of each class (Fig. 2c). Collectively, these neurons appear to

encompass the full pattern of trans-Tango-positive cells (Fig. 2b). These cell types comprise nine morphologically distinct ascending neurons and 56 interneurons. We did not detect any motor neurons directly postsynaptic to the MDNs. For the purposes of this work, we assigned these cell types provisional names starting with MT (for “MDN trans-Tango”), followed by either an A for ascending neurons or 1, 2, or 3 for interneurons in the T1, T2, or T3 segments, respectively, and finally a consecutive two-digit number (Fig. 2c).

Volumetric calcium imaging reveals cell types responsive to MDN activation. Labeling with trans-Tango neither provides information as to the strength or sign of synaptic connections, nor can it reveal cell types that are functionally responsive to the MDNs but not amongst their immediate postsynaptic partners. We therefore complemented this anatomical approach with volumetric functional imaging (Fig. 3a). We optogenetically activated the MDNs using CsChrimson²⁰ and monitored calcium responses at 1 Hz in the VNC with GCaMP6s²¹. MDN was activated with a series of 20-s red-light pulses, one per minute over a 10-min period. Responsive cells were identified using a voxel-wise analysis of covariance with a kernel that captures the dynamics of the stimulus protocol and GCaMP6s response kinetics (Fig. 3a). In initial experiments in which GCaMP6s was expressed in all neurons, or all glutamatergic neurons, we reproducibly observed both excitatory and inhibitory responses in the VNC, predominantly but not exclusively in the T3 segment (Fig. 3b and Supplementary Movie 3).

In functional imaging experiments in which GCaMP6s was broadly expressed, it was not possible to reliably identify individual responsive cells. We therefore used an iterative approach in which we screened selected lines from large collections of GAL4 or LexA drivers^{22,23}. We started with a panel of relatively broadly expressed lines, and then, for any line in which we detected MDN-responsive cells, iteratively examined successively sparser lines likely to contain these cells. Additionally, we included sparse driver lines likely to include any of the cell types identified in the trans-Tango experiments. For the sparsest lines in which a GCaMP6s response was observed, we identified the specific cell type that was MDN-responsive by matching the pattern of correlated voxels to a series of images of single cells obtained by stochastic labeling²⁴ using a driver line containing the same enhancer (Fig. 3c). These identified neurons were then manually segmented from the stochastically labeled samples.

While this iterative sampling approach inevitably fails to isolate all the MDN-responsive cells, it was sufficiently broad in scope to allow us to resolve a total of 33 morphologically distinct MDN-responsive cell types (Fig. 3d–f). We provisionally refer to these

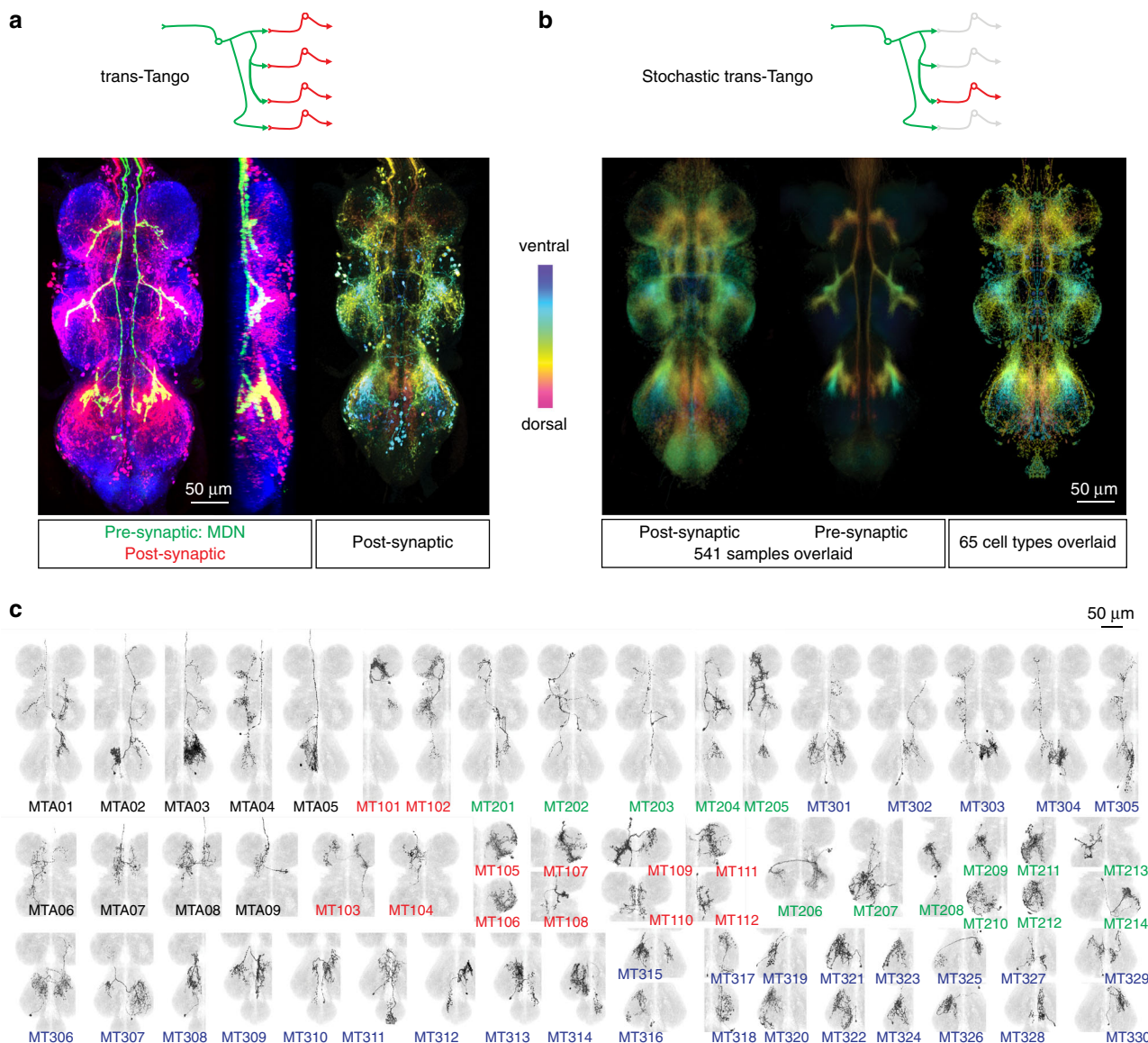


Fig. 2 Trans-Tango reveals cells postsynaptic to MDNs. **a** Top, schematic of trans-Tango labeling, showing target cell in green and trans-synaptically labeled cells in red. Bottom, an example of trans-Tango labeling of cells postsynaptic to MDNs, targeted with *MDN-1-GAL4*. Left, maximum projection confocal image of the VNC, shown in ventral and lateral views, with MDN axons in green (anti-GFP), trans-Tango labeled cells in red (anti-HA), and all synapses in blue (anti-Bruchpilot, nc82). Right, the same sample registered onto a standard VNC template, with the trans-Tango channel shown as a color-coded maximal intensity projection (colorMIP) in which color encodes the z-section in which the maximum occurs. **b** Top, schematic of stochastic trans-Tango labeling. Bottom left and middle, standard deviation projections of colorMIP images of the post- and presynaptic channels, respectively, of 541 stochastic trans-Tango samples. Bottom right, standard deviation projection of 65 types of segmented neurons and their mirror images. **c** Segmented MT cell types from stochastic trans-Tango dataset, shown as registered maximum intensity projections overlaid on the JRC2017 template VNC. Cell-type designations are colored to indicate ascending neurons (black), and interneurons with soma located in either T1 (red), T2 (green), or T3 (blue). Each cell type is given a provisional name beginning with “MT” (“MDN trans-Tango”).

cell types here as MF cells (MDN functional imaging). As for the MT cells identified with trans-Tango, the MF cells also include both interneurons (Fig. 3d) and ascending neurons (Fig. 3e), and are predominantly located in T3. Additionally, one type of MDN-responsive motor neuron was identified in the functional imaging experiments (Fig. 3f). Not surprisingly, and indeed in part due to our search strategy, there is considerable overlap amongst the cells identified by trans-Tango and by functional imaging, with a total of 20 cell types detected by both methods (Supplementary Fig. 1).

The MF cells exhibit a diverse array of responses to MDN activation (Fig. 3d–f and Supplementary Fig. 2). Most MF cell

types showed a positive calcium response upon MDN activation, as expected given that the MDNs are cholinergic, and hence excitatory, and that GCaMP6s more reliably reports excitation than inhibition. Some cells however consistently showed inhibitory responses to MDN activation. None of these inhibited cells were trans-Tango positive, and indeed would not be expected to be directly postsynaptic to the excitatory MDNs. Both the excitatory and inhibitory responses varied considerably in their amplitude and dynamics, even amongst segmentally repeated cells of the same type. For example, the MF09, MF13, and MF25 cells are each present in all three segments, yet MDN activation elicited strong activation only in the T3 MF09s, the T1

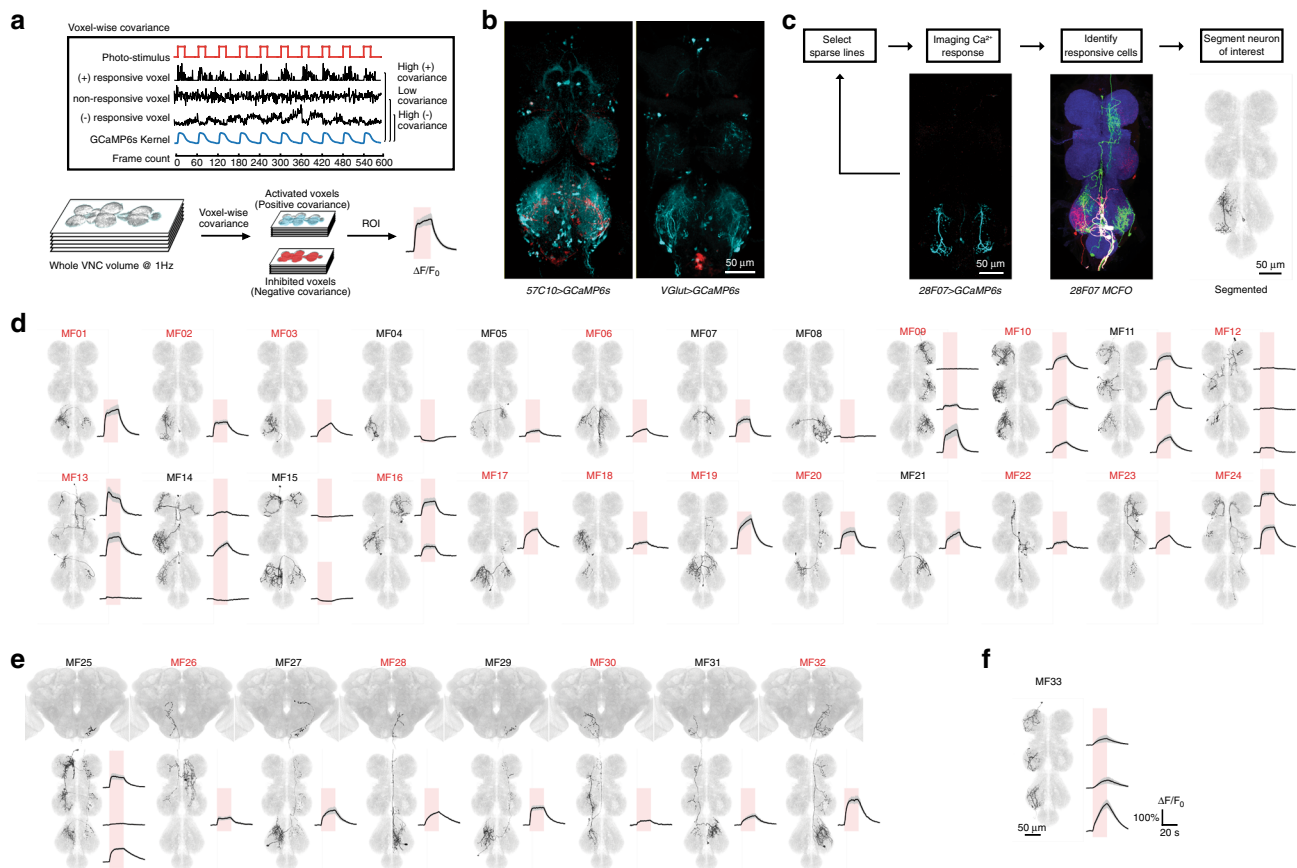


Fig. 3 MDN-responsive neurons identified by functional imaging. **a** Schematic of the functional imaging and data analysis pipeline. **b** Maximum intensity projections of imaged VNC volumes during photostimulation, using *MDN-1-GAL4* to drive Chrimson88 in MDNs. Cyan represents activated voxels; red represents inhibited voxels. See also Supplementary Movie 3. We recorded from at least 5 independent samples for each genotype and obtained similar results across the samples. **c** Top, pipeline for discovering cell types that are functionally connected to MDN. Bottom, an example showing how an MDN-responsive cell type is identified. The three images are, from left to right, a maximum intensity projection of activated voxels in the VNC of a fly in which Chrimson88 expression is driven by *MDN-1-GAL4* and GCaMP6s expression is driven by *28F07-LexA*, a multi-color flip-out (MFCO) image from the corresponding *28F07-GAL4* driver, and a single cell segmented from the MFCO image that matches the morphology of the MDN-responsive neurons. **d** Twenty-four MF interneuron types, whereby segmentally repeated cells are classified as the same cell type. Maximum intensity projections of segmented and registered images are shown on the left; averaged responses to MDN activation on the right (mean \pm s.e.m. of $n \geq 5$ samples; red shading indicates the 20 s red-light stimulus; see also Supplementary Fig. 2). Cell types labeled in red were also identified in the trans-Tango experiments (see Supplementary Fig. 1 for pairwise comparisons). **e** Eight MF ascending neuron types and their calcium responses to MDN activation. **f** The single MF motor neuron type and its calcium response to MDN activation. Each cell type in d-f is given a provisional name beginning with “MF” (“MDN functional imaging”).

and T2 MF13s, and the T1 and T3 MF25 (Fig. 3d). An even more dramatic example of segment-specific MDN responses is MF14, for which the T1 and T2 cells were excited but the T3 cells inhibited (Fig. 3d).

Several MF cell types contribute to MDN-induced backward walking. Even the sparsest driver lines we used to identify the MF cells in the functional imaging experiments typically label several additional cell types. Although these other cell types are not MDN-responsive, they may nonetheless contribute directly or indirectly to walking. This initial set of GAL4 driver lines was therefore not ideal for a functional analysis of the MF cells in backward walking, and so we instead used the split-GAL4 method^{23,25,26} to generate highly specific driver lines for selected MF cells. These lines were generated as part of a larger effort to systematically classify and genetically target each of the neuronal cell types in the leg neuropils (R.M., K.F., B.J.D., in preparation). We matched each of the segmented MF cell profiles to specific cell types defined in this systematic classification, thereby identifying a total of 82 stable split-GAL4 (SS) lines that collectively

covered 29 of the 33 MF cell types (Fig. 4a and Supplementary Fig. 3a).

We then used these split-GAL4 driver lines to determine whether genetically silencing each class of MF cell was able to suppress MDN-induced backward walking in an open arena (Fly Bowl²⁷). For this we generated flies in which CsChrimson was expressed in MDNs using a split-LexA driver, and tetanus toxin light chain²⁸ in a single class of MF cells using one of the SS lines (Supplementary Fig. 4). As a negative control we used an empty GAL4 driver (lacking an enhancer element); as positive controls we used two different MDN GAL4 drivers (*MDN-1-GAL4* and *MDN + MAN-1-GAL4*)¹¹. For each of these genotypes, we typically examined a total of ~50 flies distributed across two trials for their locomotion responses to red-light stimulation (Supplementary Fig. 3b and Supplementary Movie 4). Figure 4b shows the mean backward locomotion during the stimulus period for each of the 82 MF split-GAL4 lines and the three controls. Robust backward walking was observed upon MDN activation in negative control flies, but completely abolished in both of the positive controls (Fig. 4b). Similarly, for several MF cell types,

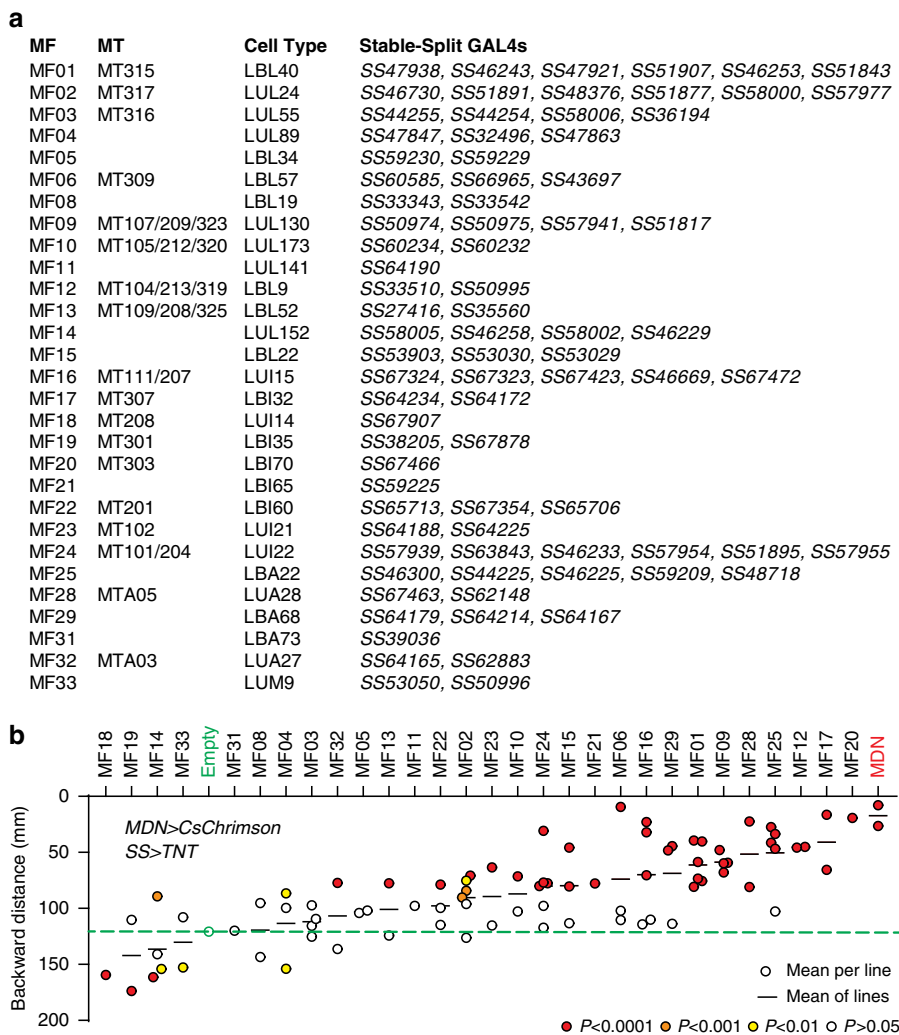


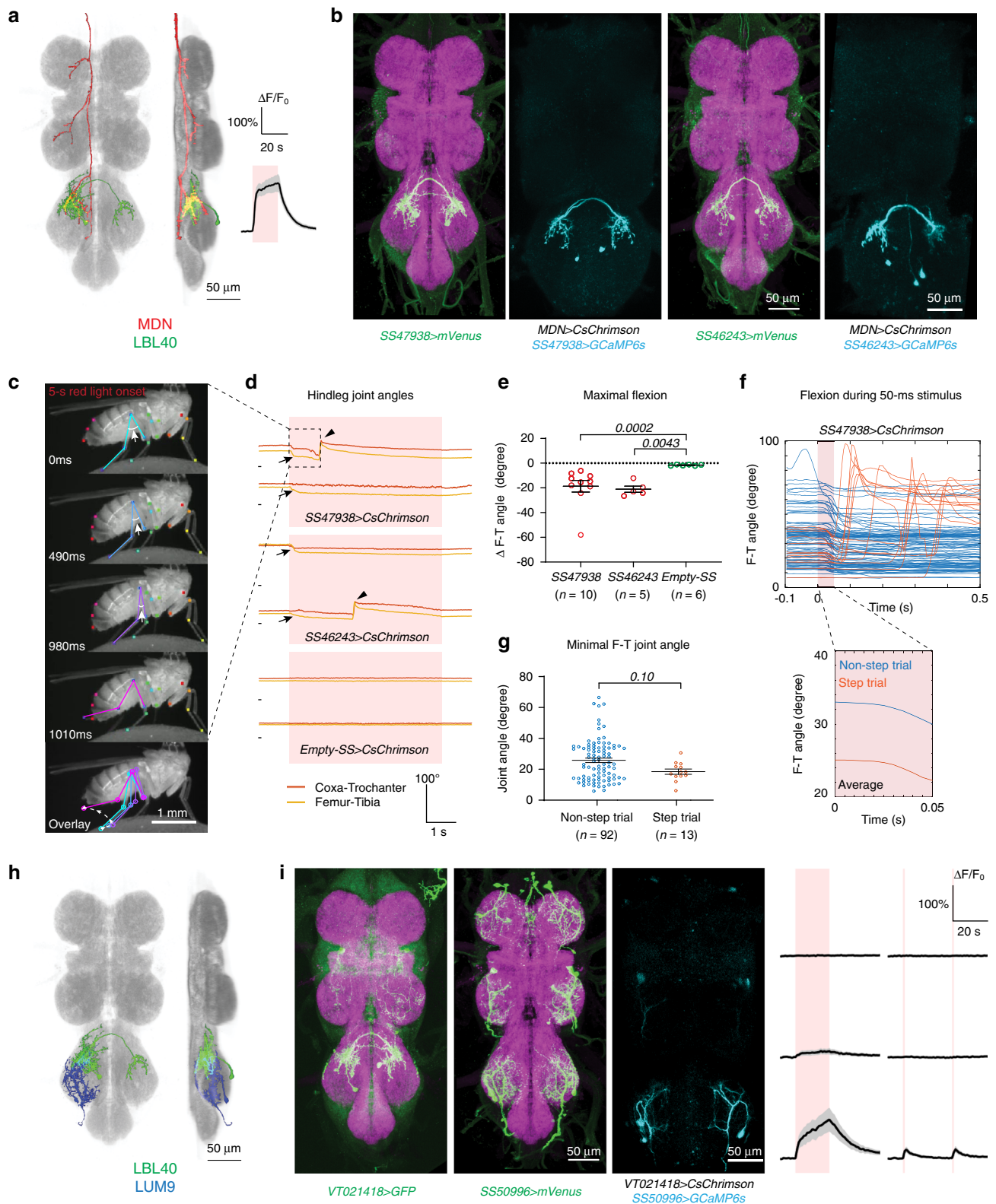
Fig. 4 Several MF cell types contribute to MDN-induced backward walking. **a** Correspondence between 29 MF cell types, their matching MT cell types, cell types identified in a systematic analysis of leg neuropil neurons, and the split-GAL4 lines that label them and were used to generate the data shown in **b**. **b** Total backward walking distance during 9 episodes of 5-s photoactivation of MDN, in flies in which a single MF cell type was silenced. Each data point represents the mean of all flies tested with a single split-GAL4 line, shaded to indicate *P* values from one-way ANOVA tests with post-hoc Dunnett’s correction for multiple comparisons. For cell types for which multiple split-GAL4 lines were tested, the mean across all lines is shown. Dashed green line marks the backward walking distance of negative control flies, for comparison. See also Supplementary Fig. 3b. and Supplementary Movie 4. Source data are provided as a Source Data file.

multiple driver lines all resulted in a strong impairment of backward walking. Some of these also exhibited defects in spontaneous forward walking (Supplementary Fig. 3b), but many specifically disrupted backward walking. Of these, we decided to focus our further analysis on two of the cell types for which we had the most SS driver lines and the most consistent reduction of backward walking: MF01, which corresponds to the LBL40 cells in our systematic classification of leg neuropil neurons, and MF09, which corresponds to LUL130. For these two cell types, a total of 6 and 4 SS driver lines, respectively, were all able to suppress MDN-induced backward walking. We next asked if and how each of these two cell types contributes to MDN’s effect on hindleg joint movements.

LBL40 neurons trigger tibia flexion via the tibia-reductor motor neurons. The LBL40 cells, identified in both the MDN trans-Tango (MT315, Fig. 2c) and functional imaging experiments (MF01, Fig. 3d and Supplementary Movie 5), are a bilateral pair of neurons specific to the T3 neuropils (Fig. 5a). They resemble the only surviving neurons of the 14B lineage²⁹. Each of

6 LBL40 split-GAL4 driver lines reduced MDN-induced backward walking in the neuronal silencing experiments (Fig. 4b). The most restricted of these lines are SS47938 and SS46243. SS47938 labels no other cells in the central nervous system, whereas SS46243 additionally labels a pair of ascending neurons (Supplementary Fig. 3a). Using these two cell-type-specific driver lines in calcium imaging experiments, we confirmed that the LBL40 neurons indeed respond to MDN activation (Fig. 5b).

If the LBL40 neurons mediate specific joint movements during MDN-induced backward walking, then optogenetic activation of these neurons in stationary flies might elicit these joint movements in isolation. We tested this prediction using tethered, decapitated flies. Decapitation removes all descending inputs to the leg motor circuits, so that any leg movements induced by optogenetic activation of leg interneurons are not obscured by movements triggered by brain activity. A tethered, decapitated fly is normally stationary, but optogenetic activation of the severed VNC projections of the MDNs induces backward walking, with its characteristically exaggerated hindleg movements (Supplementary Fig. 5).



In this decapitated fly preparation, optogenetic activation of LBL40 using either *SS47938* or *SS46243* reliably induced hindleg tibia flexion at stimulus onset (Fig. 5c, d [arrows], and e). As the stimulus persisted, the initial tibia flexion was occasionally followed by rapid leg lifting and extension to execute a full backward step cycle (arrowheads in Fig. 5d). A similar pattern of tibia flexion, followed in some cases by stepping, was also seen in a series of experiments using a shorter 50 ms stimulus (Fig. 5f and

Supplementary Movie 6). With this shorter stimulus, the stepping occurred with a variable delay and outside the stimulus window, suggesting that it is not a direct consequence of LBL40 activation. If stepping occurred, it was initiated from a small joint angle (Fig. 5g). However, there was no significant difference in the minimum angle reached in stepping versus non-stepping trials, suggesting that reaching this small angle does not automatically trigger the next swing phase (Fig. 5g).

Fig. 5 LBL40 neurons control tibia flexion. **a** Segmented and registered images of MDN (red) and LBL40 (green) from ventral and lateral perspectives, and calcium response in LBL40 upon photoactivation of MDN. Same data as in Fig. 3d, see also Supplementary Movie 5. **b** Confocal images of VNCs of two split-GAL4 lines labeling LBL40 (magenta, nc82 staining; green, anti-GFP staining of CsChrimson-mVenus reporter), and activated voxels (cyan) from calcium imaging experiments using each line. **c** Selected frames from a representative video of LBL40 activation in a tethered, decapitated fly, during a 5-s red-light stimulus from $t = 0$ ms. Arrows indicate the femur-tibia angles. Dashed line with arrows in the overlay image indicates sequence of movement. See also Supplementary Movie 6. **d** Hindleg joint angle time series, showing two representative traces for each genotype. Red shade indicates a 5-s pulse of red light. A short black line marks the origin for each trace ($t = 0$ s, 0 degrees). Arrows indicate the initial femur-tibia flexion; arrowheads mark steps. The top traces are from the video shown in **c**. **e** Maximal femur-tibia joint flexion within 1 s after red-light onset. Bars indicate mean \pm s.e.m. *P* values are shown in italics; two-tailed Mann-Whitney tests. Source data are provided as a Source Data file. **f** Top, overlaid hindleg femur-tibia joint angles from trials in which LBL40 was activated by a 50 ms light pulse. Bottom, mean joint angle traces, calculated separately for trials with and without a step. Red shading indicates the red-light stimulus. $N = 3$ flies and $n = 105$ trials. **g** Minimum femur-tibia joint angles for non-step and step trials. Bars indicate mean \pm s.e.m. *P* values are shown in italics, two-tailed Mann-Whitney test. Source data are provided as a Source Data file. **h** Registered segmented image of LBL40 (green), LUM9 (blue), and all synapses (gray, nc82). **i** Confocal images of VNCs of a *LexA* line labeling LBL40 and *SS50996*, labeling LUM9 (green, anti-GFP staining of a *myr-GFP* or CsChrimson-mVenus reporter; magenta, nc82), and activated voxels (cyan) from calcium imaging of LUM9 upon LBL40 activation. Traces show the averaged responses for LUM9 to LBL40 activation (mean \pm s.e.m., $N = 6$ flies), upon either a single 20-s stimulus or two 1-s light pulses (red shading).

These photoactivation experiments suggest that LBL40 is a premotor neuron for tibia flexion. The single class of motor neuron identified in our functional imaging experiments, MF33, has a morphology that matches that of the motor neurons innervating the tibia-reductor muscle^{30,31}, which is responsible for tibia flexion^{32,33}. In our systematic classification of neurons in the leg neuropils, we designated these as the LUM9 neurons (R. M., K.F., and B.J.D., in preparation). They are present in each segment, but upon MDN stimulation are preferentially activated in T3 (Fig. 3f). We confirmed that the LUM9 neurons are indeed the tibia-reductor motor neurons by examining their muscle innervation in the leg (Supplementary Fig. 6a). As expected, optogenetic activation of the LUM9 neurons induced hindleg tibia flexion, albeit without the re-extension that was observed with LBL40 activation (Supplementary Fig. 6b–d). Calcium imaging experiments demonstrated that the T3 LUM9 neurons are activated upon stimulation of either the LBL40 neurons (Fig. 5h, i) or the MDNs (Supplementary Fig. 6e), and a GRASP experiment³⁴ suggested that they are direct synaptic partners of the LBL40 cells (Supplementary Fig. 6f).

We conclude from these experiments that LBL40 activates the LUM9 neurons to induce hindleg tibia flexion. LBL40 and LUM9 are thus candidates to provide the hindleg power stroke during the stance phase of backward walking.

LUL130 neurons trigger leg lifting. Like the LBL40 neurons, the LUL130 neurons were also identified in both the MDN trans-Tango (MT323, Fig. 2c) and functional imaging experiments (MF09, Fig. 3d and Supplementary Movie 7), and are also required for robust MDN-induced backward walking (Fig. 4b). LUL130 neurons are segmentally repeated local interneurons, but were most strongly activated by MDN in T3 (Fig. 6a). The T2 LUL130 neurons responded less strongly to MDN activation, and no response was detected in the T1 LUL130s. The most restricted split-GAL4 lines we obtained for these neurons are *SS50974* and *SS50975*. *SS50974* labels only the T3 cells, whereas *SS50975* labels cells in all three thoracic segments (Fig. 6b). Neither driver labels any other cells in the CNS (Supplementary Fig. 3a). We confirmed with these drivers that both the T2 and T3 LUL130 neurons are activated upon optogenetic stimulation of the MDNs (Fig. 6b; note that *SS50975* drives weaker expression in T3 than in T1 and T2).

Using decapitated and tethered flies, we found that optogenetic activation of LUL130 induces lifting and a swing-like movement of the leg. With the *SS50974* driver, only the hindlegs were lifted (Fig. 6c–e and Supplementary Movie 8); with *SS50975*, all six legs were lifted (Fig. 6d, e). We examined the hindleg lifting induced

by *SS50974* activation more closely and observed that a single brief (5 ms) pulse of red-light stimulation elicited a coordinated sequence of leg movements involving all three joints and resembling the swing phase of backward walking (Fig. 6f). Using the *SS50975* driver to activate the LUL130 neurons in all three segments, we found that a longer red-light stimulus (5 s) resulted in an alternating pattern of stepping across all six legs. Despite the simultaneous optogenetic activation of all LUL130 neurons, the legs stepped in a coordinated pattern similar to that typically observed in forward walking, with the fore- and hindlegs on one side of the body in phase with the midlegs on the other (Fig. 6g, h and Supplementary Movie 9; refs. 35,36). These data suggest that the LUL130 neurons initiate swing phase, which then follows the normal pattern of both inter-joint and interleg coordination.

LBL40 and LUL130 function in the stance and swing phases of backward walking. Finally, we sought to test the functional hypotheses we derived from the activation experiments: that LBL40 and LUL130 act at distinct timepoints during the backward stepping cycle, with LBL40 providing the hindleg power stroke during stance phase and LUL130 neurons subsequently initiating swing phase. We tested these hypotheses by silencing either the LBL40 or LUL130 cells in tethered flies induced to walk backwards by MDN activation, and tracking the resulting hindleg joint movements. Such experiments required an optogenetic silencer and an activator that could be independently controlled with minimal crosstalk. We found that we could best achieve this by stimulating CsChrimson with 660 nm red light and the neuronal silencer GtACR2³⁷ with 470 nm blue light. With these tools, we established a protocol using tethered and decapitated flies in which CsChrimson was expressed in the MDNs and GtACR2 in either the LBL40 or LUL130 neurons. Positive control flies expressed GtACR2 in the MDNs; negative controls used an “empty” split-GAL4 driver that resulted in no GtACR2 expression. Each fly was subject to a series of control and experimental trials (Fig. 7a). Control trials consisted solely of a 25-s red-light stimulus to activate the MDNs. Experimental trials additionally included a 10-s blue-light stimulus to silence the LBL40 or LUL130 neurons, applied 10-s after the onset of the red-light stimulus.

In positive control flies, MDN-induced backward walking was fully suppressed by optogenetic silencing of the MDNs themselves (Fig. 7b). Conversely, negative control flies were unaffected by the blue-light stimulus in experimental trials (Fig. 7c). When LBL40 neurons were silenced, the power stroke appeared to be weakened, as suggested by the reduced speed and amplitude of tibia flexion, and hence a slight delay in the initiation of swing

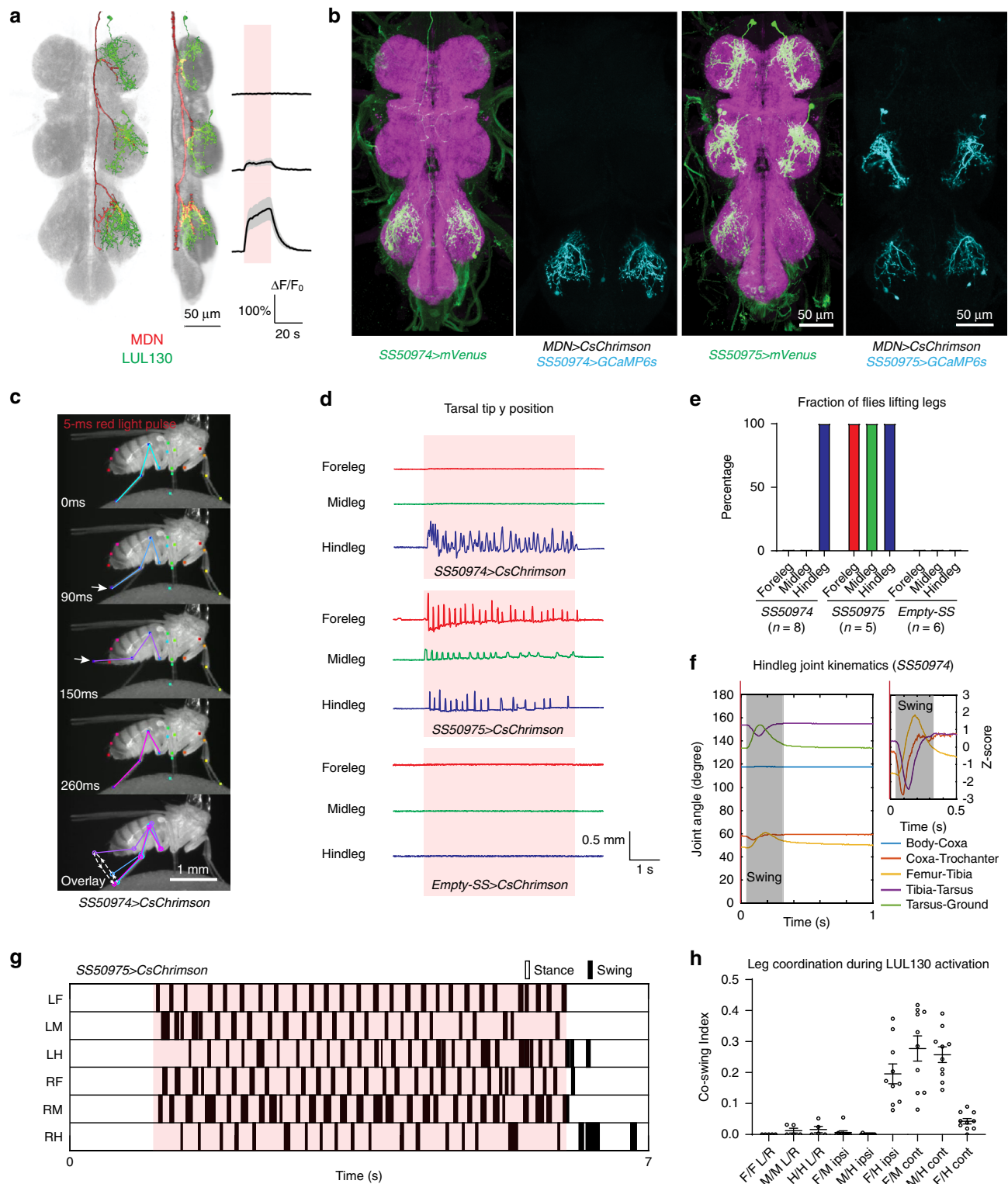


(Fig. 7c and Supplementary Movie 6). In contrast, when LUL130 neurons were silenced, the power stroke was unaffected, as judged by the initial speed of tibia flexion. However, in these LUL130-silenced flies, the leg appeared to be stuck in stance phase, with the tibia flexing to a much greater extent before swing was eventually initiated (Fig. 7c and Supplementary Movie 10).

We quantified these effects by measuring the femur-tibia joint angle during each step in the 10-s blue-light stimulus period of experimental trials and the corresponding periods of control trials

for the same fly (Fig. 7d). We aligned these curves by time-point of their maxima, which typically occurred in the middle of the short swing phase, 20–30 ms before the start of stance phase. From these curves we then determined, for each fly, the average initial speed and maximum extent of tibia flexion during stance phase, and the frequency of stepping, across all experimental and control trials (Fig. 7e–g). This analysis confirmed our initial impression that LBL40-silenced flies, but not LUL130-silenced flies, had a reduced speed of tibia flexion during the blue-light

Fig. 6 LUL130 neurons trigger leg lifting. **a** Segmented and registered images of MDN (red) and LUL130 (green) from ventral and lateral perspectives, and calcium responses of LUL130 upon MDN activation. Same data as in Fig. 3d, see also Supplementary Movie 7. **b** Confocal images of VNCs of two split-GAL4 lines labeling LUL130 (magenta, nc82 staining; green, anti-GFP staining of CsChrimson-mVenus reporter), and activated voxels (cyan) from calcium imaging experiments using each line. **c** Selected frames from a representative video of LUL130 activation in a tethered, decapitated fly upon a 5-ms red-light stimulus applied at $t = 0$ ms. Arrows indicate the femur-tibia angles. Dashed line with arrows in the overlay image indicates sequence of movement. See also Supplementary Movie 8. **d** Representative traces of tarsal tip positions for each leg. Red shade indicates a 5-s pulse of red light. **e** Percentage of flies lifting each leg. **f** Left, averaged hindleg joint angles upon photoactivation of LUL130 by 5-ms red-light pulses, starting at 0 ms. Gray indicates the inferred swing phase. Right, z-scores of coxa-trochanter, femur-tibia and tibia-tarsus angles from the same data, highlighting the phase relationships between joints. $N = 3$ flies and $n = 100$ trials. **g** Representative footfall pattern during a continuous 5-s photoactivation of LUL130 (red shading). LF, LM, LR, RF, RM, RH designate left and right fore-, mid- and hindlegs, respectively. See also Supplementary Movie 9. **h** Leg coordination during 5-s photoactivation of LUL130, quantified as a co-swing index (the total time both legs are in swing divided by the time either leg is in swing). Bars indicate mean \pm s.e.m. $N = 5$ flies ($n = 5$ intrasegmental leg pairs, $n = 10$ intersegmental pairs). F foreleg, M midleg, H hindleg, L left, R right, ipsi ipsilateral, cont contralateral. Source data are provided as a Source Data file.

stimulus (Fig. 7e). In LBL40-silenced flies, the femur-tibia joint was less flexed than in negative control flies; in LUL130-silenced flies it was more flexed (Fig. 7f). Both LBL40- and LUL130-silenced flies took fewer steps (Fig. 7g), presumably, however, for different reasons. In LBL40-silenced flies, the late transition to swing phase is explained by a slower stroke (Fig. 7e), not a greater degree of flexion (Fig. 7f). In LUL130-silenced flies, the late initiation of swing correlated with a greater flexion (Fig. 7f), not a slower stroke (Fig. 7e). Similar results were obtained when we compared the blue-light stimulus period of experimental trials to the pre- or post-blue-light stimulus periods of the same trials, rather than to control trials (Supplementary Fig. 7a, b). We also found that the increase in hindleg stepping that results from tarsal amputation (Fig. 1i, j) is similarly suppressed by LUL130 silencing, suggesting that these oscillations, like normal steps, are centrally driven (Supplementary Fig. 7c).

These data thus confirm our hypotheses from the activation experiments. LBL40 and LUL130 neurons mediate two distinct aspects of MDN-induced backward walking. LBL40 neurons function in tibia flexion, providing the power stroke during stance phase. LUL130 neurons facilitate leg lifting at the end of stance phase to initiate swing and complete the stepping cycle.

Discussion

Backward walking triggered by the MDNs is an excellent model for exploring how descending command-like neurons produce abrupt but coordinated changes in motor circuit output. The data presented here indicate that MDN acts primarily on the T3 motor circuits, such that the hindlegs become the major driving force in backward walking. The T1 and T2 motor circuits also receive MDN input, but the backward stepping of the fore- and midlegs is primarily dependent upon proprioceptive signals generated as the hindlegs propel the body backwards. Through a combination of trans-synaptic tracing and functional imaging, we identified over 30 neuronal cell types targeted by MDN—the majority of them in T3. Amongst these are the LBL40 and LUL130 neurons, which act at separate stages in the hindleg stepping cycle. LBL40, a premotor neuron for tibia flexion, mediates the power stroke in stance phase. LUL130, an interneuron that triggers leg lifting, is responsible for the initiation of swing. Together, these data suggest that the MDNs do not act solely, if at all, through a high-level bistable switch that controls the stepping direction^{38,39}, but rather individually modulate each of the diverse motor outputs needed for coordinated backward walking.

Tibia flexion and femur elevation are the most prominent hindleg joint movements during the stance phase of backward walking—the two movements largely occurring in synchrony to fold up the leg, thereby pulling the body backwards. The LBL40 neurons, which are specific to T3, flex the hindleg tibia by activating LUM9, one of the tibia flexor motor neurons. Femur

elevation may be mediated through other MDN-effector neurons, possibly included amongst the MF and MT cell types we have not yet examined in detail. There may also be some mechanical coupling between the two joints, as we often observed femur elevation (flexion of the coxa-trochanter joint) when tibia flexion was induced by activating either LBL40 or LUM9. Such mechanical coupling between tibia flexion and femur elevation has been observed in the stick insect⁴⁰. Femur elevation was, however, generally weaker and less reliable than tibia flexion in the LBL40 activation experiments, suggesting that it is not the primary function of these neurons.

LUM9 is one of a large group of motor neurons that innervate the tibia flexor muscles. It most closely resembles the “slow” tibia flexor motor neurons, which have the lowest activation threshold and highest spiking rate but generate the weakest force³³. It is possible that LBL40 also activates other tibia flexor motor neurons, but the *ex vivo* nature of our preparation or the limited sensitivity of our imaging method hampered our ability to detect these responses. Indeed, silencing of LBL40 suppressed MDN-induced backward walking, whereas silencing of LUM9 did not. This suggests that at least some other tibia flexor motor neurons may also be involved in backward walking.

In behavioral assays, the fly typically backs up for several steps when it encounters an obstacle, despite receiving only a transient mechanosensory stimulus. However, upon artificial activation of MDNs, the fly walks backwards only so long as the stimulus persists^{11,12}. These results suggest that circuits in the brain convert an acute mechanosensory stimulus into tonic activation of MDNs. This conclusion is supported by *in vivo* functional imaging experiments, which showed a sustained calcium response in the MDNs during bouts of backward walking⁴¹. The LBL40 and LUM9 neurons, in contrast, are presumably only phasically active, becoming silent when the leg pauses or is re-extended. The timing of LBL40 and LUM9 activation must therefore be determined by other inputs, most likely including proprioceptive signals from the same as well as other legs^{42–44}. One such input may be phasic inhibition from proprioceptive neurons that are activated when the tibia nears full flexion⁴⁵.

To complete the stepping cycle, the retracted leg must initiate swing and return to its extended position. Several factors act together to initiate swing, including the position of the leg, the unloading of the leg, and the loading of other legs^{42,43,46–48}. Some or all of these factors might lead to activation of the LUL130 neurons, which trigger leg lifting and initiate swing phase. It is interesting to note that the LUL130 neurons are present in all three segments but are most strongly activated by MDN in T3. Perhaps, during backward walking, the relative weighting or timing of the factors that initiate swing are most dramatically altered for the hindleg, and MDN effects these changes. For example, when walking forwards, the hindleg initiates swing from

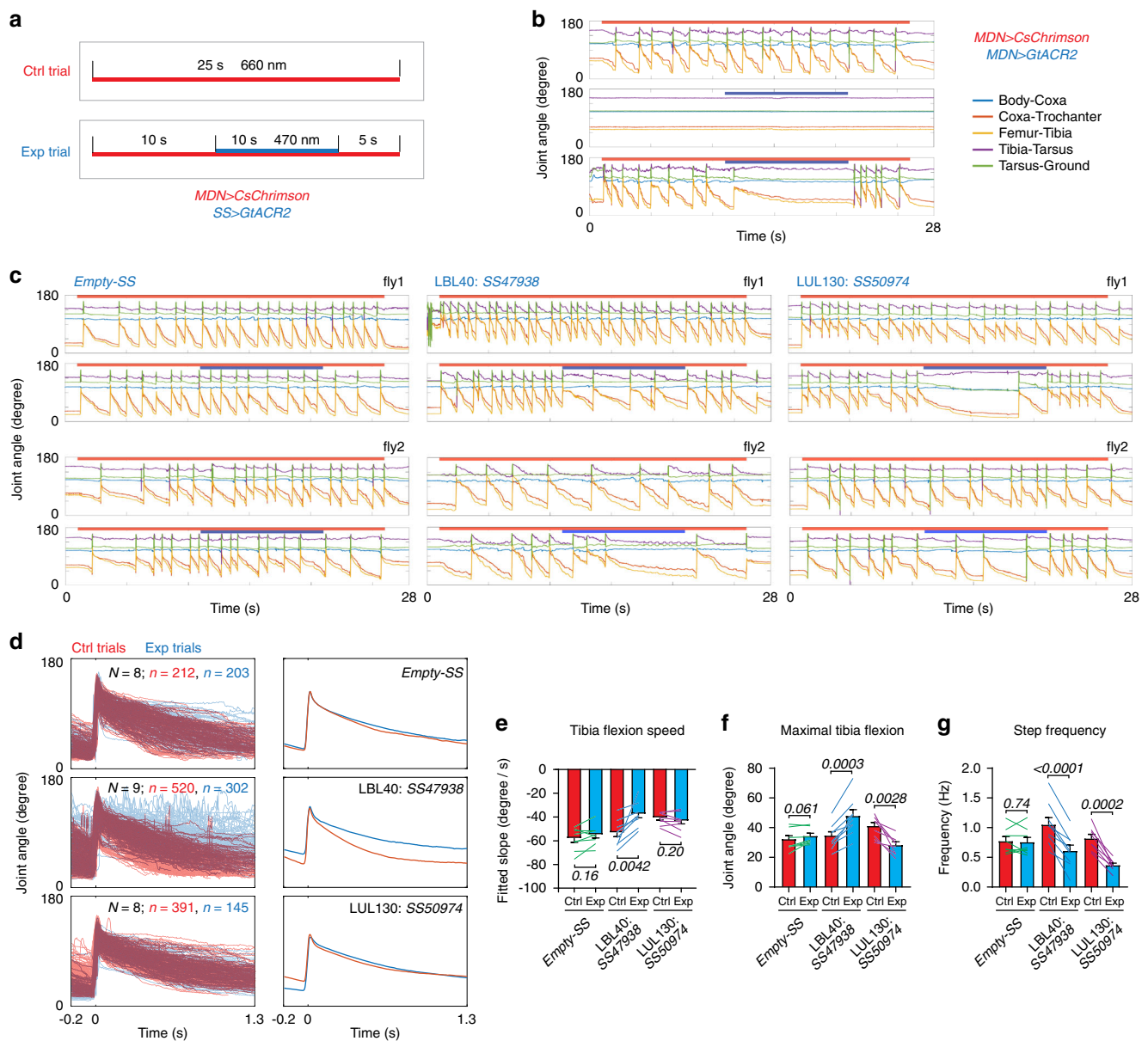


Fig. 7 LBL40 and LUL130 function in the stance and swing phases of backward walking. **a** Experimental protocol. Each fly was subject to the same number of control (Ctrl) and experimental (Exp) trials. Red bar indicates red-light stimulus; blue bar indicates blue-light stimulus. **b** Representative hindleg joint angle time series for positive control flies expressing both CsChrimson and GtACR2 in MDN, and stimulated with either red and blue light alone, or both. **c** Representative hindleg joint angle time series for flies of the indicated genotypes. See also Supplementary Movies 10 and 11. **d** Left: overlaid femur-tibia joint angle from all steps during the 10-s blue-light stimulus in experimental trials (blue), and the corresponding period in control flies (red). Right: average of all steps for experimental (blue) and control (red) trials. Before averaging, individual traces were truncated if another step occurred within the 1.5 s time window. **e–g** Slope of femur-tibia joint angle change (**e**) and minimum angle (**f**) during stance phase, and step frequencies (**g**) during the 10-s blue-light stimulus period of experimental trials and the corresponding period of control trials. All data are shown as mean \pm s.e.m. across all N flies, with colored lines pairing experimental and control values for the same fly. P values are shown in italics, two-tailed paired t -tests. Source data are provided as a Source Data file.

an extended position; when walking backwards, swing is initiated from the folded position. Further insight into the circuit mechanisms that initiate swing should come from mapping proprioceptive and other inputs to LUL130 neurons, and determining how MDN activity shapes LUL130's responses to these inputs. Such circuit mapping may also help elucidate the role of LUL130 in interleg coordination. The recent release⁴⁹ of an electron-microscope volume of the VNC should greatly facilitate these circuit reconstruction efforts.

We propose that, as for LBL40, it is primarily the intra- and interleg sensory feedback signals that ensure the phasic activation

of LUL130 neurons despite tonic input from MDNs. But it is also possible that inhibitory pathways entirely within the central motor circuits also contribute to the alternating phasic activation of LBL40 and LUL130. These central mechanisms might include reciprocal feedforward inhibition. Feedforward inhibition from LUL130 to LBL40 could relax the tibia flexor during the return stroke, while inhibition from LBL40 to LUL130 may help keep leg grounded throughout its power stroke. In this scenario, LBL40 and LUL130 may be integral components of a central pattern generator for stepping, the neuronal basis of which has been elusive in insects.

Explanations of how descending inputs from the brain control motor circuits have focused on two alternative modes of action: population coding versus command neurons^{50,51}. The population model emphasizes the fact that a large number of descending neurons are often simultaneously active during a motor task⁵², and that each individual type of descending neuron may have a low-level, highly localized effect on a small number of muscles⁵³. In this model, coordinated changes in motor output reflect the collective action of many different descending neurons, and only certain patterns of activity in these descending neurons—a population code—are capable of eliciting a behaviorally meaningful motor output. The command neuron model, in contrast, notes the profound and coordinated motor responses that can sometimes result from the activation of just a single class of descending neuron⁵⁴. Because the motor responses elicited by a single command-type neuron can involve the coordinated activation of many different muscles, command-type descending neurons are generally thought to implement a relatively high-level control of motor circuits.

Computational models of backward walking in insects have posited the existence of bistable control switch for leg motor circuits, the setting of which determines whether motor rhythms are generated in a pattern that produces forward or backward walking^{38,39}. Because this switch coordinately effects multiple motor outputs, it represents a high-level control embedded within the leg motor circuits. If such high-level directional switches exist in the *Drosophila* leg neuropils, then MDN, as a command-type descending neuron, could act by flipping these switches into the “backward” mode. Our data suggest, however, that this is not the case. We found that, of the two MDN-output neurons we examined in detail, each controls a discrete element of backward walking: hindleg tibia flexion during stance (LBL40) and leg lifting to initiate swing (LUL130). Many MDN-output neurons remain to be characterized, and it is possible that some of these may yet emerge as components of a high-level circuit switch coordinately effecting multiple motor features. Our data suggest, however, that at least some of MDN’s control is exerted at a lower level, close to motor output, and in a highly localized manner. The neuronal networks that control walking evidently operate in at least two stable states—one producing forward walking, the other backward walking. We propose that MDN may act through a distributed set of outputs, rather than a central control switch, to flip network dynamics into the backward state. In this model, MDN functions as a command-type neuron not because it acts at a higher level in motor control, but because the many discrete low-level changes it effects alter motor circuit dynamics so as to produce a clear and coordinated transition to backward walking.

In light of these findings, we suggest that, in both the command-type and population coding scenarios, descending neurons can act in a highly localized, modulatory fashion, exerting their influence at the level of single muscles or muscle groups. In this view, it is not difficult to envision how evolution could shift the descending control of motor circuits up or down the continuum from a single-unit command-type control to a more combinatorial population-based control. Duplication of descending neurons and diversification of their outputs would result in a shift towards a more distributed control system, which might be favored under conditions in which flexibility or precision are advantageous. Conversely, a single descending neuron that initially has a highly specific and localized impact may become more potent over the course of evolution as it acquires new connections. An evolutionary shift in this direction might be favored if efficiency and reliability are more important than flexibility and precision.

In conclusion, we propose that there is no fundamental mechanistic distinction between a command type of control and a

population type of control. The former does not necessarily impinge upon motor circuits at a higher level than the latter. Rather, we suggest that these two opposing models are merely extremes on a continuum, and that both can be implemented through the distributed, low-level modulation of motor circuits. Where any single class of descending neuron falls on this spectrum depends, proximally, on the extent to which the many local modulations sum to produce a coordinated and behaviorally-relevant motor response, and ultimately, on the evolutionary trade-off between flexibility and efficiency.

Methods

Fly stocks. See Supplementary Table 1 for genotypes of *Drosophila* used in this study, and Supplementary Table 2 for full genotypes of flies used for experiments presented in each Figure. All flies were raised on standard semi-defined media at 25 °C, 50% relative humidity and 12–12 h light cycle except for flies used in the trans-Tango dataset, which were raised at 18 °C. All flies for behavioral experiments or functional imaging were sexed within 2 days after eclosion and aged on fresh food supplemented with all-trans retinal (0.2 mM) and kept in the dark (food tube wrapped with foil). All flies for immunohistochemistry were sexed within 2 days after eclosion and aged on fresh food. Both males and females were used in Fly Bowl experiments, CsChrimson activation experiments using tethered flies, and immunohistochemistry. For calcium imaging, MDN amputation and GtACR2 neuronal epistasis experiments, only females were used. For all behavioral experiments and immunostainings except for trans-Tango, 3–8-day-old adult flies were used. For calcium imaging, 3–20-day-old adult flies were used. For trans-Tango experiments, 15–40 day-old flies (raised at 18 °C) were used.

Behavioral assays. Neuronal epistasis experiments in Fig. 4b and Supplementary Fig. 3b were conducted as in ref.¹³ using the Fly Bowl setup²⁷. Briefly, video recordings were performed under backlit infrared LEDs at 30 fps with a resolution of 1024 × 1024 pixels. A group of ~25 flies were loaded into the bowl-shaped arena and allowed to walk for 60 s before the first optogenetic stimulation. The first 45 s of this period were used to compute the spontaneous forward walking speed in Supplementary Fig. 3b. A red-light source at 627 nm wavelength illuminated the entire arena uniformly to activate CsChrimson. Each red-light stimulus was 5 s in duration and in 60-s intervals (onset to onset). In total nine episodes of red-light stimuli were applied in one experiment with three consecutive episodes for each of 3 intensity levels from low to high: 0.158, 0.288, and 0.456 mW/mm².

Flies were anaesthetized using a cold block set to 0–1 °C and placed in a fly-shaped groove. A drop of adhesive “Not-A-Glue” (Bondic, Canada) was applied to the notum of the fly using a thin metal wire. A bent metal pin fixed on one end of a rod was lowered by a manual manipulator to gently touch the adhesive. Then the adhesive was cured by LED light (provided with the adhesive). When decapitated flies were used, we cut off fly’s head with fine scissors (Fine Science Tools, CA) before gluing. The tethering process normally takes less than 3 min. The tethered flies were then given a styrofoam ball (~5 mm diameter) to hold before experiments to keep them from struggling. The rod with fly tethered is then attached on a manual manipulator in the ball setup. The compressed air supporting the ball was carefully adjusted to the minimal level that can spin the polypropylene ball (PP ball, 6 mm in diameter, Spherotech GmbH, Germany) without the fly stepping on it. The fly was then moved carefully to the top of the PP ball supported by a custom-built ball holder (Electronics workshop, Zoological Institute, University of Cologne). A top camera was used to monitor the fly’s position on ball so that the fly can be properly centred. From the side view, we used the minimal projected area of the wings as a sign to adjust the roll of the fly. A custom-built infrared-LED ring (wavelength: 880 nm, Electronics workshop, Zoological Institute, University of Cologne) was positioned around the camera lens for illumination. A few initial videos were acquired at 200 fps with a resolution of 464 × 464 pixels from a CameraLink camera VC-2MC-M340 (Vieworks, Korea) equipped with a telecentric lens TEC-M55 (Computar, USA). For majority of the experiments, a USB3 camera GS3-U3-23S6M-C (FLIR, Canada) equipped with a 75 mm zoom lens with extension tube (to further increase the zoom so that the field of view on the 1/1.2 inch CMOS chip is ~12 mm in width) and an infrared filter was controlled by Spinnaker software (FLIR, Canada) to acquire videos from the side view of fly. For the FLIR camera, videos were initially acquired at 200 fps at a resolution of 960 × 800 and then cropped and downsized to 464 × 464 to match the videos taken from the Vieworks camera. Data from both Vieworks and FLIR cameras were analyzed by the same DeepLabCut model. Only for SS50975 activation experiments, two Basler acA1920-155um cameras (Basler AG, Germany) equipped with Infinitix 1 × 94 mm lens (with a 5.8 mm aperture retainer ring and an infrared filter; Infinity Photo-optical Company, CO) were used under control of Pylon software (Basler AG, Germany) to take videos simultaneously from both sides of the body. In those experiments, frame rate was 200 fps and frame size was 960 × 480. Movies from Basler cameras were manually scored. An Arduino UNO (Arduino.cc) was used to synchronize cameras and optogenetic stimuli. A custom built 660 nm diode laser with fibre coupling (Electronics workshop, Zoological Institute, University of Cologne) was used to deliver the red-light stimulus for

CsChrimson. A fiber coupled 470 nm LED (M470F1, Thorlabs, NJ) controlled by a custom LED driver (QBI Workshop, Australia) was used to deliver the blue-light stimulus for GtACR2. Multimode optical fibers ($\text{\O}200 \mu\text{m}$, 0.39 NA for red light; $\text{\O}200 \mu\text{m}$, 0.50 NA for blue light; Thorlabs, NJ) were used to deliver light to the flies (both with SMA coupling to source and clean-cut bare end pointing to sample). The red-light intensity used for 50-ms (Fig. 5f, g and Supplementary Movie 6), 5-s (Fig. 1, Fig. 5c–e, Fig. 6d, e, g, h, Supplementary Fig. 5, Supplementary Fig. 6c, d, and Supplementary Movies 1, 2, 9) and 25-s pulses (Fig. 7, Supplementary Fig. 7, and Supplementary Movies 10, 11) was $\sim 0.73 \text{ mW/mm}^2$ and the intensity for 5-ms pulses (Fig. 6c, Fig. 6f and Supplementary Movie 8) was $\sim 3.8 \text{ mW/mm}^2$. The blue light intensity (Fig. 7, Supplementary Fig. 7, and Supplementary Movies 10, 11) was $\sim 0.11 \text{ mW/mm}^2$. For *MDN > CsChrimson* activation experiments, we first allowed the flies to walk freely in order to capture spontaneous forward walking episodes and then triggered backward walking using a 5-s constant red-light stimulus. For tarsal amputation experiments, we first recorded from intact flies and then cut off the tarsal tip at the middle of the tarsus on cold block with a pair of fine scissors before recording again from the same flies with identical protocol. For *SS > GtACR2* neuronal epistasis experiments, we first tested if a decapitated fly could walk backwards steadily during the 25-s red-light stimulus. Only flies that showed stable baseline backward walking throughout the 25-s window were further tested. We performed exactly the same number of control trials and experimental trials in an alternating sequence on each fly.

Immunohistochemistry. Immunohistochemistry was performed on the central nervous system (CNS) dissected from adult flies, following protocols in <https://www.janelia.org/project-team/flylight/protocols>. Samples for MCFO, mVenus and GFP staining and tdTomato/TNT double staining were DPX mounted. Samples for trans-Tango and GRASP experiments were mounted in Vectashield (Vector Laboratories, CA). Confocal stacks were obtained at $1 \mu\text{m}$ intervals using an LSM 710 microscope (Carl Zeiss AG, Germany) with a $\times 20$ objective, or a $\times 40$ objective for MCFOs.

For trans-Tango experiments, the flies were aged at 18°C for 15–40 days before dissection. We found in pilot experiments that *MDN-1 > trans-Tango* flies showed only sparse or no labeling of postsynaptic cells, but a *UAS-CsChrimson-mVenus* transgene enhanced the trans-Tango signal dramatically even in the absence of a red-light stimulus or retinal food. For stochastic trans-Tango, two genotypes with different *hs-FLP* transgenes were used (see Supplementary Table 2 for full genotypes), and the data pooled. Flies were heat-shocked at 37°C for 1–3 sessions each lasting 2 h at various stages from first-instar larvae to mid-pupae. We diversified the heat-shock protocol in order to get sparse labeling as well as high coverage of postsynaptic cells. When multiple heat shocks were performed, they were spaced by at least 1 day. More than a thousand samples were dissected and stained, of which 541 samples with sparse to medium expression were registered against a VNC template (JRC2017, ref. 19) and further analyzed. The antibodies and concentrations used in those experiments were as follows: primary rabbit anti-GFP (Merck/Millipore AB-3080P, 1:1000), primary rat anti-HA (Roche 11867423001, 1:100), primary mouse anti-Bruchpilot (Developmental Studies Hybridoma Bank nc82, 1:20), secondary Alexa Fluor 488 goat anti-rabbit (Thermo Fisher Scientific A-11034, 1:500), secondary Alexa Fluor 555 goat anti-rat (Thermo Fisher Scientific A-21434, 1:800), and secondary Alexa Fluor 647 goat anti-mouse (Thermo Fisher Scientific A-21236, 1:500).

For mVenus and GFP staining, the antibodies used were as follows: primary rabbit anti-GFP (Thermo Fisher Scientific A-11122, 1:1000), primary mouse anti-Bruchpilot (1:30), secondary Alexa Fluor 488 goat anti-rabbit (1:800) and secondary Alexa Fluor 568 goat anti-mouse (Thermo Fisher Scientific A-11031, 1:400). For MCFO, the majority of experiments were hybrid immunohistochemistry/chemical tag stainings, following the protocol listed in the abovementioned website (see also ref. 55). The antibodies and dyes used were Cy2 SNAP-tag ligand (Luke Lavis, JRC, $10 \mu\text{L/mL}$ for final concentration of $2 \mu\text{M}$), primary rat anti-FLAG Tag (Novus Biologicals NBP1-06712, 1:200), primary rabbit anti-HA Tag (Cell Signalling Technologies 3724 S, 1:300), secondary ATTO647N goat anti-rat (Rockland 612-156-120, 1:300), secondary AF594 donkey anti-rabbit (Jackson ImmunoResearch 711-585-152, 1:500), and DL550 mouse anti-V5 (AbD Serotec MCA1360D550GA, 1:500). A few experiments were immunohistochemistry only and only differed from the hybrid protocol in that mouse anti-Bruchpilot (1:30) and Cy2 Goat anti-mouse (Jackson ImmunoResearch 711-585-152, 1:600) were used instead of the Cy2 SNAP-tag ligand. For tdTomato and TNT double labeling, the antibodies used were as follows: primary rabbit anti-TNT (Statens Serum Institute 65873, 1:3000), primary rat anti-RFP (Chromotek 5f8-20, 1:500), primary mouse anti-Bruchpilot (1:30), secondary Alexa Fluor 488 goat anti-rabbit (Thermo Fisher Scientific A-11034, 1:800), secondary Cy3 goat anti-rat (Jackson ImmunoResearch 112-165-167, 1:1000), and secondary Cy5 goat anti-mouse (Jackson ImmunoResearch 115-175-166, 1:1000). For GRASP experiments, we used polyclonal antibody rabbit anti-GFP (AB-3080P, 1:1000) followed by secondary Alexa Fluor 647 goat anti-rabbit (Thermo Fisher Scientific A-21245, 1:500) to label GFP1-10 and imaged the live fluorescence for reconstituted GFP and tdTomato, which was co-expressed with GFP11. For leg muscle innervation in Supplementary Fig. 6a, the flies were fixed in 4% paraformaldehyde overnight at 4°C . After five times of 15-min washing in 0.3% PBST, we removed the legs

with forceps and mounted them in Vectashield. We then imaged live fluorescence of mVenus and RFP for nerves and muscles respectively.

Calcium imaging. All calcium imaging experiments were performed on ex vivo preparations of the fly CNS. The entire CNS of female flies were dissected in extracellular solution comprising (in millimoles): 103 NaCl, 3 KCl, 5 N-Tris (hydroxymethyl)methyl-2-aminoethanesulfonic acid (TES), 8 trehalose, 10 glucose, 26 NaHCO_3 , 1 NaH_2PO_4 , 2 CaCl_2 , and 4 MgCl_2 (pH near 7.3 when bubbled with 95% (vol/vol) O_2 and 5% (vol/vol) CO_2 (carbogen)). The extracellular solution was bubbled with carbogen and prechilled on ice before dissection. After dissection, the tissues were quickly transferred to a custom chamber filled with fresh extracellular solution and stuck to a fresh glass coverslip placed at the bottom of the chamber. The chamber was then placed on the stage under microscope and constantly perfused with fresh extracellular solution bubbled with carbogen throughout the experiments. The room temperature was controlled at 23°C .

Two-photon imaging was performed on a Thorlabs Bergamo II microscope equipped with a Galvo-Resonant scanner (Thorlabs, NJ). A piezo objective focus module with $400 \mu\text{m}$ travel distance (Physik Instrumente GmbH & Co. KG, Germany) was used to control an Olympus XLUMPLFN $\times 20$ water immersion objective (Olympus, Japan). A Mai Tai DeepSee Ti:Sapphire laser (Spectra-Physics, CA) was tuned to 920 nm for two-photon stimulation. A Pockels Cell (Conoptics Inc., CT) was used to control the laser intensity and ramp it while scanning deeper into the tissue. A 617 nm LED source (M617F1, Thorlabs, NJ) controlled by a LED driver (DC4104, Thorlabs, NJ) was coupled to the two-photon light path to deliver the optogenetic stimuli through the objective. A 594 nm long pass dichroic was used pass the 920 nm laser and 617 nm red light and reflect fluorescence from the sample to a pair of GaAsP PMTs (Hamamatsu, Japan). A 562 nm long pass dichroic was placed between the two PMTs and a 525/50 nm band pass filter was placed in front of the PMT that was used to detect light from GCaMP. During an imaging session, an Arduino UNO (Arduino.cc) was used to trigger and synchronize two-photon imaging and optogenetic stimulus.

All imaging experiments were performed under the streaming mode in Thorimage software (Thorlabs, NJ). We scanned 27 effective slices spaced by $6 \mu\text{m}$ plus three flyback slices (discarded during analysis) to cover a whole VNC volume. The imaging frame was set to 512×1024 pixels and zoomed to just cover the full VNC. Under such a condition, the imaging speed was approximately 30 frames or 1 VNC volume per second. The laser power on sample was ranging from 1.5 to 20 mW dependent on the driver line's strength and depth of scanning plane. We performed recording sessions containing 60 volumes (~ 1 min) and gave the sample either 1 red-light stimulus lasting 20 s (onset from imaging start: 10 s; see Fig. 3d–f, Fig. 5a, Fig. 6a, Supplementary Fig. 2a, and Supplementary Fig. 6a, e) or 2 stimuli each lasting 1 s (onset from imaging start: 10 s and 40 sec; see Fig. 5i, Supplementary Fig. 2b, and Supplementary Fig. 6e). Each red-light stimulus contains a train of 5 ms pulses at 50 Hz. The light power (not peak power; 25% duty cycle as a result of 5 ms pulses at 50 Hz) measured at the sample was 0.81 mW. Given the field of view under the $\times 20$ objective was approximately 0.9 mm in diameter, we calculated the light intensity was approximately 1.27 mW/mm^2 . In a typical experiment, we repeat 10 such 60-s sessions on each sample, with a 15-s interval between sessions.

Functional imaging screen. Starting from relatively broad lines and patterns we saw from trans-Tango experiments, we selected ~ 300 GAL4 or LexA lines from the GMR²² and VT collections²³ with progressively sparser expression patterns until we can pinpoint any single cell types from the calcium imaging patterns responding to MDN activation. We used *MDN-1-GAL4 (VT044845-ZpGAL4DBD in attP40, VT050660-p65ADZp in attP2, ref. 11)* to drive expression of Chrimson88 specifically in MDNs when we imaged LexA lines. We used a split *MDN-LexA (VT049484-ZpLexADBD in JK22c, VT050660-p65ADZp in attP2, ref. 12)* to drive expression of CsChrimson in MDNs when we imaged GAL4 lines. The latter used the same enhancer combinations as the *MDN + MAN-1-GAL4*¹¹ and expressed in both MDNs and MANs but no other central neurons. To exclude the possibility that MANs were responsible for activating a given cell type, we also used a *MDN-LexA (VT044845-LexA, ref. 13)*, which is broader but does not label MAN, to confirm the response we saw from a positive GAL4 line is attributable to MDN activation. For the screen, we typically imaged two samples per line with the 20-s photostimulation protocol and rescreened the few lines that showed inconsistent patterns. Combining the results from both GAL4 and LexAs, we identified 33 cell types of which the calcium imaging patterns can be clearly matched to a neuron from MCFO patterns driven by lines containing the same enhancer as those we used for calcium imaging. We considered cells in different segments as segmentally repeating cell types if they shared common genetic drivers and had similar morphology. Many cell types were hit by multiple GAL4 or LexA lines (see Supplementary Data). We selected at least one line for each cell type and expanded the sample numbers to at least five, with which we applied both 20-s and 1-s stimulation protocols, as shown in Fig. 3 and Supplementary Fig. 2.

Neuron segmentation. To segment an MF neuron type, we obtained stochastic labeling images using GAL4 lines containing the same enhancers that were used for calcium imaging to drive expression of a MCFO reporter²⁴ (see Supplementary

Table 2 for full genotypes). To segment an MT neuron type, we used images from the stochastic trans-Tango dataset in Fig. 1b. In both cases, we selected images that showed relatively sparse patterns surrounding the neuron of interest. For MDN (Fig. 5a, Fig. 6a and Supplementary Fig. 6e), we used an image from the MDN stochastic labeling dataset reported in ref.¹³. All VNC images were nonrigidly registered⁵⁶ to JRC2017 template¹⁹ and brains to JFRC2013 template⁵⁷. Using the software VVD Viewer^{19,58,59}, we rendered the registered image stacks in 3D and manually masked other neurons co-labeled in the image and segmented out the neuron of interest.

Generation of split-GAL4 lines targeting MF cell types. As part of a large effort to systematically targeting cell types in leg neuropils (R. M., K. F., and B. D. *in preparation*), we used images of targeted cell types to generate Color-MIP masks and search through the images of GMR and VT lines¹⁹ to obtain enhancers that may contain the cell type of interest. We made combinations of these enhancers pairwise in split-GAL4 halves^{23,25} and tested their expression patterns by immunostaining. For those pairs that sparsely labeled the neuron types of interest, we stabilized them by double balancing the AD and DBD halves to obtain the SS lines.

Quantification and statistical analysis. From the 4-D raw data of imaging, we first concatenated 10 of the 60-s recording sessions on the same sample to create a 600-frame hyperstack containing $1024 \times 512 \times 27$ voxels. We then performed motion-correction on each of the 27 slices using the NoRMCorre algorithm⁶⁰. We also generated two GCaMP6s kernels for both the 20-s and 1-s stimuli. To do this, we manually defined ROIs on neurons that showed strong activation with short delay and calculated the $\Delta F/F_0$. By averaging multiple such ROIs, we created smooth response curves that capture typical response dynamics to our MDN activation protocols. We then calculated the cross-covariance between the time series of each voxel and the corresponding kernel using the Matlab function “xcov” with the “maxlag” parameter set to 5. This parameter allowed us to detect time-shifted responses that could come from polysynaptic connections to MDN. The cross-covariance analysis resulted in 11 values for each voxel. We used the maximal positive values or 0 if all 11 were negative to reconstruct an image stack that represents the “activated” voxels (cyan in Fig. 3b, c, Fig. 5a, i, Fig. 6a and Supplementary Fig. 6e). Likewise, we used the minimal negative values or 0 if all 11 were positive to reconstruct an image stack that represents the “inhibited” voxels (red in Fig. 3b). We compared these images with immunostainings of the same or other driver lines to identify neurons that respond to MDN activation or select sparser lines to narrow down the pattern. We also used these images as a guide to define ROIs on neurons of interest to calculate $\Delta F/F_0$. We manually defined ROIs using the freehand or polygon tools in Fiji⁶¹. For each sample, the ROI was defined on a single imaging plane that showed strong responses and large areas for the given neuron type. For neuron types containing multiple cells with overlapping neurites, the ROIs may cover multiple neurons of the same type. For neuron types containing a single neuron and the counterparts in each hemisphere do not overlap, we defined the ROIs on the neuron that showed stronger response in each sample. To calculate $\Delta F/F_0$, we took the averaged intensity in each ROI from frame 2–9 for each of the 60-s imaging sessions as the baseline F_0 . For each sample, we then calculated averaged $\Delta F/F_0$ of the 10 imaging sessions. The averaged $\Delta F/F_0$ from multiple samples were used to compute the response curves (see Fig. 3d–f, Fig. 5a, i, Fig. 6a, and Supplementary Fig. 6e) and quantify the maximal responses (see Supplementary Fig. 2) for each cell type.

Movies recorded from the Fly Bowl were tracked and analyzed using a pipeline based on Ctrax⁶². Briefly, all flies were first tracked in each frame throughout the video. Forward/backward speed (in Ctrax output reported as “du_ctr”) were further analyzed to generate results in Fig. 4b and Supplementary Fig. 3b. This only considers the centroid’s speed component in parallel with the animal’s heading, excluding any sideways component (perpendicular to the fly’s heading). Spontaneous forward walking and triggered backward walking distance for each fly was computed individually and results for all flies from multiple assays of each genotype were pooled. For forward walking distance, the total forward/backward distance for flies walked in the initial 45 s (15 s prior to the first episode of red-light stimulus) of the assay was computed. For backward walking distance, the accumulative backward distance (a backward speed threshold $>=1.5$ mm/s was applied as in ref.¹³) during the nine episodes of red-light stimuli (3 red-light levels, three episodes each level, 5 s each episode, in total 45 s) was computed. In both cases, the walking distance was calculated by integrating the forward/backward speed frame by frame throughout the time windows without considering the flies’s position in the arena.

An artificial neural network was trained using DeepLabCut software^{16,63} to mark four joints and the tarsal tip of each leg, two antenna and three points on the abdomen (as illustrated in Fig. 1a) of a fly either walking on ball or being suspended. In total 780 frames out of 39 videos sized 464 by 464 were manually marked as the training set. The frames were carefully chosen to represent flies under different conditions and performing different motor tasks and a few pilot networks were trained and evaluated to extract some of the frames included in the final training set. The final network was trained by this training dataset from the default resnet101 weights for 1030000 iterations. All the videos analyzed by the network were overlaid with the markings (see Fig. 1a) for manual quality control. Tracking errors were usually limited to very few frames. Time series of joint angles

(as illustrated in Fig. 1b) and tarsal tip y positions were batch computed and plotted to facilitate human inspection. For the dataset in Fig. 1b–h, only videos that did not contain obvious tracking errors for any joints were used. For all cases in which femur-tibia and/or coxa-trochanter angles were plotted and quantified, manual quality control was applied on the relevant joints to exclude videos that had obvious mistracking. Z-scored tarsal tip y positions were then used to detect the peak of each swing phase (referred to as “swing peak” hereafter) by Matlab function “findpeaks”. For all cases where individual steps were extracted or stepping frequency were quantified, manual quality control was applied to correct the errors in swing peak detection.

For Fig. 1b–h, we used a dataset containing one episode of spontaneous forward walking and one episode of optogenetically triggered backward walking for each of the seven flies. Manual proofreading ensured errors in joint position tracking and swing peak detection (see above) were minimal for this dataset. Using the swing peaks, we aligned all the steps across flies and averaged the tarsal tip positions and joint angles to plot the data in Fig. 1c, d. For Fig. 1d, the 0.5 s time window contained the swing peak at frame 50, 49 preceding frames, and 50 subsequent frames. If a neighbouring swing peak falls into this time window, we truncated the step. So for each step, the boundary was either the abovementioned time window or shortly after the previous swing peak or before the next swing peak. The grey areas indicating swing phase were determined by the inflection point of the positions of tarsal tips of the averaged steps. The step size was defined as the distance between Anterior Extreme Position (AEP) and Posterior Extreme Position (PEP). The swing stroke amplitude was defined as the distance between the Dorsal Extreme Position (DEP) and the line segment connecting AEP and PEP. The joint angle range was defined as the maximum minus the minimum of each joint angle during a step. To plot Fig. 1e–h, we calculated the mean of relevant parameters from all steps for each fly, which represented a single data point in these plots.

For Fig. 1i, j we used a dataset containing 5–10 trials each before and after tarsal amputation for each fly. The amputated legs technically did not have a stance phase, but they showed oscillations resembling steps. So we refer to the highest tarsal tip position during each oscillation as swing peak here for simplicity. We detected and manually corrected the timing of swing peaks of all steps for intact legs or all oscillations for amputated legs. Using this information, we could calculate the averaged frequency of steps or oscillations for each leg in each fly across multiple trials, which represent single data points in Fig. 1j. The step frequency in Supplementary Fig. 5c and Supplementary Fig. 7c was quantified in the same way.

For Fig. 5e and Supplementary Fig. 6d, we used a dataset that contained a single trial for each fly, in which the tracking of coxa-trochanter and femur-tibia joint angles in hindlegs had minimal errors. Given many of the flies with LBL40 activated showed red-extension of tibia following initial flexion, we quantified the maximal flexion in 1 s after optogenetic stimuli onset before such red-extension.

For Fig. 5f, g we used 50-ms light pulses spaced by at least 1 s to activate the neuron. We aligned 105 trials from three flies by the stimulus onset and overlaid the femur-tibia angle to plot Fig. 5f. We then divided all the trials by whether red-extension of tibia followed the initial flexion and plotted the minimal femur-tibia joint angle following each stimulus to generate Fig. 5g.

For Fig. 6e, we manually scored whether a leg showed repeated stepping under 5-s red-light stimuli for each leg of the flies in this dataset. For Fig. 6f, we used 5-ms light pulses spaced by at least 1 s to activate the neuron. We aligned 100 trials from three flies by the stimulus onset and calculated the average of each joint angle from all trials. We took the averaged joint angles during the first 0.5 s after stimulus onset to calculate the Z-score (number of standard deviations from the mean). For Fig. 6g, we manually scored every frame as either stance or swing for each leg. We can use this information to calculate the co-swing index to plot Fig. 6h. The co-swing index was defined by the total co-swing time of two limbs divided by the total time either of the two limbs were in swing during the optogenetic stimulation. This dataset included one video with 5-s stimuli for each of the 5 flies.

For Fig. 7d–g and Supplementary Fig. 7a, b, we used a dataset containing the same number of control trials and experimental trials for each fly, following the protocol illustrated in Fig. 7a. We detected and manually corrected all swing peaks (see above) for hindlegs. We then aligned all steps that happened during the specified time windows (10-s window delayed by 10 s after red-light onset for Figs. 7d–g and 5-s windows as illustrated in Supplementary Fig. 7a, b) for each genotype and experimental condition using the swing peaks. We used a 300-frame (1.5 s) time window and placed the swing peak at frame 40 (200 ms before the swing peak was shown) to plot Fig. 7d. We truncated steps at boundaries of the abovementioned time windows or eight frames (40 ms) before the next swing peak if the next step arose within the 1.5 s time window. For Fig. 7e–g, we calculated the mean of relevant parameters in all steps for each fly and condition. For Fig. 7e, we applied the Matlab function “fit” with input parameter “poly1” on the declining phase (from the maximal femur-tibia angle position to the boundary of the 1.5 s window, i.e., 1.3 s after the swing peak) of averaged femur-tibia angles in all steps for each fly and condition. We used the linearly fitted slope as a quantification of tibia flexion speed. For Fig. 7f, we calculated the averaged minimal femur-tibia joint angle shortly before each swing peak of all steps for each fly and condition. For Fig. 7g, we took the reciprocal of the average duration (time between two neighbouring swing peaks) of all steps for each fly and condition to calculate the step frequency.

Details about statistical tests and sample sizes are indicated in the Figure or Figure legends. All statistical analysis were performed in GraphPad Prism 8.0. For

all confocal images, we performed at least 2 (for images in Supplementary Fig. 3a) and typically 3–5 (for images shown in other figures) independent samples and we obtained similar results across the trials.

Reporting summary. Further information on research design is available in the Nature Research Reporting Summary linked to this article.

Data availability

Confocal images of the central nervous systems of split-GAL4 lines used in this study are available at <http://splitgal4.janelia.org/cgi-bin/splitgal4.cgi>. Other datasets generated during the current study are available from the corresponding author on reasonable request. Source data are provided with this paper.

Received: 7 July 2020; Accepted: 5 November 2020;

Published online: 02 December 2020

References

- Orlovsky, G. N., Deliagina, T. G. & Grillner, S. *Neuronal Control of Locomotion. From Mollusc to Man* (Oxford University Press, 1999).
- Edwards, D. H. & Prilutsky, B. I. in *Neurobiology of Motor Control: Fundamental Concepts and New Directions* (eds S. L. Hooper & A. Büschges) Ch. 9, (Wiley, 2017).
- Le Gal, J.-P., Dubuc, R. & Smarandache-Wellmann, C. in *Neurobiology of Motor Control: Fundamental Concepts and New Directions* (eds S. L. Hooper & A. Büschges) Ch. 10, (Wiley, 2017).
- Pflüger, H.-J. & Grillner, S. in *Neurobiology of Motor Control: Fundamental Concepts and New Directions* (eds S. L. Hooper & A. Büschges) Ch. 7, (Wiley, 2017).
- Bidaye, S. S., Bockemuhl, T. & Buschges, A. Six-legged walking in insects: how CPGs, peripheral feedback, and descending signals generate coordinated and adaptive motor rhythms. *J. Neurophysiol.* **119**, 459–475 (2018).
- Mu, L. & Ritzmann, R. E. Interaction between descending input and thoracic reflexes for joint coordination in cockroach: I. Descending influence on thoracic sensory reflexes. *J. Comp. Physiol. A Neuroethol. Sens Neural Behav. Physiol.* **194**, 283–298 (2008).
- Lemon, R. N. Descending pathways in motor control. *Annu. Rev. Neurosci.* **31**, 195–218 (2008).
- Buschmann, T., Ewald, A., von Twickel, A. & Buschges, A. Controlling legs for locomotion—insights from robotics and neurobiology. *Bioinspir Biomim.* **10**, 041001 (2015).
- Rosenbaum, P., Schmitz, J., Schmidt, J. & Buschges, A. Task-dependent modification of leg motor neuron synaptic input underlying changes in walking direction and walking speed. *J. Neurophysiol.* **114**, 1090–1101 (2015).
- Rosenbaum, P., Wosnitzer, A., Buschges, A. & Gruhn, M. Activity patterns and timing of muscle activity in the forward walking and backward walking stick insect *Carausius morosus*. *J. Neurophysiol.* **104**, 1681–1695 (2010).
- Bidaye, S. S., Machacek, C., Wu, Y. & Dickson, B. J. Neuronal control of *Drosophila* walking direction. *Science* **344**, 97–101 (2014).
- Sen, R., Wang, K. & Dickson, B. J. TwoLumps ascending neurons mediate touch-evoked reversal of walking direction in *Drosophila*. *Curr. Biol.* **29**, 4337–4344 (2019).
- Sen, R. et al. Moonwalker Descending Neurons mediate visually evoked retreat in *Drosophila*. *Curr. Biol.* **27**, 766–771 (2017).
- Carreira-Rosario, A. et al. MDN brain descending neurons coordinately activate backward and inhibit forward locomotion. *elife* **7**, e38554 (2018).
- Berendes, V., Zill, S. N., Buschges, A. & Bockemuhl, T. Speed-dependent interplay between local pattern-generating activity and sensory signals during walking in *Drosophila*. *J. Exp. Biol.* **219**, 3781–3793 (2016).
- Mathis, A. et al. DeepLabCut: markerless pose estimation of user-defined body parts with deep learning. *Nat. Neurosci.* **21**, 1281–1289 (2018).
- Ritzmann, R. E. & Zill, S. N. *Control of Locomotion in Hexapods* (Oxford University Press, 2019).
- Talay, M. et al. Transsynaptic mapping of second-order taste neurons in flies by trans-Tango. *Neuron* **96**, 783–795 (2017).
- Otsuna, H., Ito, M. & Kawase, T. Color depth MIP mask search: a new tool to expedite Split-GAL4 creation. Preprint at <https://www.biorxiv.org/content/10.1101/318006v1> (2018).
- Klapoetke, N. C. et al. Independent optical excitation of distinct neural populations. *Nat. Methods* **11**, 338–346 (2014).
- Chen, T. W. et al. Ultrasensitive fluorescent proteins for imaging neuronal activity. *Nature* **499**, 295–300 (2013).
- Jeñett, A. et al. A GAL4-driver line resource for *Drosophila* neurobiology. *Cell Rep.* **2**, 991–1001 (2012).
- Tirian, L. & Dickson, B. J. The VT GAL4, LexA, and split-GAL4 driver line collections for targeted expression in the *Drosophila* nervous system. Preprint at <https://www.biorxiv.org/content/10.1101/198648v1> (2017).
- Meissner, G. W. et al. An image resource of subdivided *Drosophila* GAL4-driver expression patterns for neuron-level searches. Preprint at <https://www.biorxiv.org/content/10.1101/2020.05.29.080473v1> (2020).
- Dionne, H., Hibbard, K. L., Cavallaro, A., Kao, J. C. & Rubin, G. M. Genetic reagents for making split-GAL4 lines in *Drosophila*. *Genetics* **209**, 31–35 (2018).
- Luan, H., Peabody, N. C., Vinson, C. R. & White, B. H. Refined spatial manipulation of neuronal function by combinatorial restriction of transgene expression. *Neuron* **52**, 425–436 (2006).
- Robie, A. A. et al. Mapping the neural substrates of behavior. *Cell* **170**, 393–406 (2017).
- Sweeney, S. T., Brodie, K., Keane, J., Niemann, H. & Okane, C. J. Targeted expression of tetanus toxin light-chain in *Drosophila* specifically eliminates synaptic transmission and causes behavioral defects. *Neuron* **14**, 341–351 (1995).
- Shepherd, D., Sahota, V., Court, R., Williams, D. W. & Truman, J. W. Developmental organization of central neurons in the adult *Drosophila* ventral nervous system. *J. Comp. Neurol.* **527**, 2573–2598 (2019).
- Baek, M. & Mann, R. S. Lineage and birth date specify motor neuron targeting and dendritic architecture in adult *Drosophila*. *J. Neurosci.* **29**, 6904–6916 (2009).
- Soler, C., Daczewska, M., Da Ponte, J. P., Dastugue, B. & Jagla, K. Coordinated development of muscles and tendons of the *Drosophila* leg. *Development* **131**, 6041–6051 (2004).
- Miller, A. In *Biology of Drosophila* (ed. Demerec) 420–534 (1950).
- Azevedo, A. W. et al. A size principle for recruitment of *Drosophila* leg motor neurons. *elife* **9**, e56754 (2020).
- Gordon, M. D. & Scott, K. Motor control in a *Drosophila* taste circuit. *Neuron* **61**, 373–384 (2009).
- Wosnitzer, A., Bockemuhl, T., Dubbert, M., Scholz, H. & Buschges, A. Inter-leg coordination in the control of walking speed in *Drosophila*. *J. Exp. Biol.* **216**, 480–491 (2013).
- DeAngelis, B. D., Zavatore-Veth, J. A. & Clark, D. A. The manifold structure of limb coordination in walking *Drosophila*. *elife* **8**, e46409 (2019).
- Mohammad, F. et al. Optogenetic inhibition of behavior with anion channelrhodopsins. *Nat. Methods* **14**, 271–274 (2017).
- Schilling, M. & Cruse, H. Decentralized control of insect walking: a simple neural network explains a wide range of behavioral and neurophysiological results. *PLoS Comput. Biol.* **16**, e1007804 (2020).
- Toth, T. I., Knops, S. & Daun-Gruhn, S. A neuromechanical model explaining forward and backward stepping in the stick insect. *J. Neurophysiol.* **107**, 3267–3280 (2012).
- Fischer, H., Schmidt, J., Haas, R. & Buschges, A. Pattern generation for walking and searching movements of a stick insect leg. I. Coordination of motor activity. *J. Neurophysiol.* **85**, 341–353 (2001).
- Chen, C. L. et al. Imaging neural activity in the ventral nerve cord of behaving adult *Drosophila*. *Nat. Commun.* **9**, 4390 (2018).
- Cruse, H. What mechanisms coordinate leg movement in walking arthropods? *Trends Neurosci.* **13**, 15–21 (1990).
- Durr, V., Schmitz, J. & Cruse, H. Behaviour-based modelling of hexapod locomotion: linking biology and technical application. *Arthropod Struct. Dev.* **33**, 237–250 (2004).
- Lam, T. & Pearson, K. G. The role of proprioceptive feedback in the regulation and adaptation of locomotor activity. *Adv. Exp. Med. Biol.* **508**, 343–355 (2002).
- Mamiya, A., Gurung, P. & Tuthill, J. C. Neural coding of leg proprioception in *Drosophila*. *Neuron* **100**, 636–650 (2018).
- Bucher, D., Akay, T., DiCaprio, R. A. & Buschges, A. Interjoint coordination in the stick insect leg-control system: the role of positional signaling. *J. Neurophysiol.* **89**, 1245–1255 (2003).
- Dallmann, C. J., Hoinville, T., Durr, V. & Schmitz, J. A load-based mechanism for inter-leg coordination in insects. *Proc. Biol. Sci.* **284**, 20171755 (2017).
- Zill, S. N., Keller, B. R. & Duke, E. R. Sensory signals of unloading in one leg follow stance onset in another leg: transfer of load and emergent coordination in cockroach walking. *J. Neurophysiol.* **101**, 2297–2304 (2009).
- Maniates-Selvin, J. T. et al. Reconstruction of motor control circuits in adult *Drosophila* using automated transmission electron microscopy. Preprint at <https://www.biorxiv.org/content/10.1101/2020.01.10.902478> (2020).
- Heinrich, R. Impact of descending brain neurons on the control of stridulation, walking, and flight in orthoptera. *Microsc. Res. Tech.* **56**, 292–301 (2002).
- Cande, J. et al. Optogenetic dissection of descending behavioral control in *Drosophila*. *elife* **7**, e34275 (2018).
- Kristan, W. B. Jr. & Shaw, B. K. Population coding and behavioral choice. *Curr. Opin. Neurobiol.* **7**, 826–831 (1997).

53. Gonzalez-Bellido, P. T., Peng, H., Yang, J., Georgopoulos, A. P. & Olberg, R. M. Eight pairs of descending visual neurons in the dragonfly give wing motor centers accurate population vector of prey direction. *Proc. Natl Acad. Sci. USA* **110**, 696–701 (2013).
54. Kupfermann, I. & Weiss, K. R. Command neuron concept. *Behav. Brain Sci.* **1**, 3–10 (1978).
55. Meissner, G. W. et al. Optimization of fluorophores for chemical tagging and immunohistochemistry of *Drosophila* neurons. *PLoS ONE* **13**, e0200759 (2018).
56. Jefferis, G. S. et al. Comprehensive maps of *Drosophila* higher olfactory centers: spatially segregated fruit and pheromone representation. *Cell* **128**, 1187–1203 (2007).
57. Aso, Y. et al. The neuronal architecture of the mushroom body provides a logic for associative learning. *elife* **3**, e04577 (2014).
58. Wan, Y., Otsuna, H., Chien, C. B. & Hansen, C. An interactive visualization tool for multi-channel confocal microscopy data in neurobiology research. *IEEE Trans. Vis. Comput. Graph* **15**, 1489–1496 (2009).
59. Wan, Y., Otsuna, H., Chien, C. B. & Hansen, C. FluoRender: an application of 2D image space methods for 3D and 4D confocal microscopy data visualization in neurobiology research. *IEEE Pac. Vis. Symp.* 201–208 (2012).
60. Pnevmatikakis, E. A. & Giovannucci, A. NoRMCorre: An online algorithm for piecewise rigid motion correction of calcium imaging data. *J. Neurosci. Methods* **291**, 83–94 (2017).
61. Schindelin, J. et al. Fiji: an open-source platform for biological-image analysis. *Nat. Methods* **9**, 676–682 (2012).
62. Branson, K., Robie, A. A., Bender, J., Perona, P. & Dickinson, M. H. High-throughput ethomics in large groups of *Drosophila*. *Nat. Methods* **6**, 451–457 (2009).
63. Nath, T. et al. Using DeepLabCut for 3D markerless pose estimation across species and behaviors. *Nat. Protoc.* **14**, 2152–2176 (2019).

Acknowledgements

We thank the Janelia FlyLight, Fly Facility, Project Technical Resources teams, QBI infrastructure, microscopy, and IT teams and Samuel Kelly for technical assistance, Allan Wong for technical advice, and the Bloomington *Drosophila* Stock Center, Gerry Rubin, Vivek Jayaraman, David Anderson, Julie Simpson, Adam Claridge-Chang, Gilad Barnea, and Richard Mann for fly strains. We thank Josh Lillis and other members of the Dickson group at Janelia and the van Swinderen group at QBI for comments on the manuscript, and Bruno van Swinderen at QBI for co-mentorship of K.F. This work was supported by funding from the Howard Hughes Medical Institute, the NHMRC, the ARC, and a University of Queensland Major Equipment and Infrastructure grant.

Author contributions

K.F. and B.J.D. conceived the study and wrote the manuscript, with contributions from all other authors. R.S. performed some of the fly-on-ball experiments, R.M. generated the split-GAL4 lines, M.D. and T.B. designed and manufactured core parts for the setup of high-speed video tracking of flies on ball under the supervision of A.B. K.F. performed all other experiments and analyzed all the data.

Competing interests

The authors declare no competing interests.

Additional information

Supplementary information is available for this paper at <https://doi.org/10.1038/s41467-020-19936-x>.

Correspondence and requests for materials should be addressed to K.F. or B.J.D.

Peer review information *Nature Communications* thanks Chris Doe, Terufumi Fujiwara, and Pavan Ramdya for their contributions to the peer review of this work.

Reprints and permission information is available at <http://www.nature.com/reprints>

Publisher's note Springer Nature remains neutral with regard to jurisdictional claims in published maps and institutional affiliations.



Open Access This article is licensed under a Creative Commons Attribution 4.0 International License, which permits use, sharing, adaptation, distribution and reproduction in any medium or format, as long as you give appropriate credit to the original author(s) and the source, provide a link to the Creative Commons license, and indicate if changes were made. The images or other third party material in this article are included in the article's Creative Commons license, unless indicated otherwise in a credit line to the material. If material is not included in the article's Creative Commons license and your intended use is not permitted by statutory regulation or exceeds the permitted use, you will need to obtain permission directly from the copyright holder. To view a copy of this license, visit <http://creativecommons.org/licenses/by/4.0/>.

© The Author(s) 2020